Analytic Characterization of a Class of 3-Contact Frictional Equilibrium Postures in 3D Gravitational Environments

Yizhar Or and Elon Rimon*

Dept. of Mechanical Engineering, Technion, Israel

Abstract *Quasistatic legged locomotion over uneven terrains requires characterization of the mechanism's feasible equilibrium postures. This paper characterizes the feasible equilibrium postures of mechanisms supported by three frictional point contacts in a three-dimensional gravitational environment, for a subclass of contact arrangements, called* **tame***, for which the friction cones lie above the plane spanned by the contacts. The kinematic structure of the mechanism is lumped into a single rigid body $\mathcal{B}$ having the same contacts with the environment and a variable center of mass. The equilibrium postures associated with a given set of contacts become the center-of-mass locations of $\mathcal{B}$ that maintain a feasible equilibrium with respect to gravity. The paper establishes the relations between the feasible equilibrium region and the classical support polygon principle. For tame 3-contact arrangements, the paper identifies and characterizes geometrically three types of boundary curves of the feasible equilibrium region, where two of them are obtained is closed-from, and the third is given implicitly as a solution of a set of nonlinear equations, which can be traced numerically. The three types of boundary curves are then associated with the onset of three different modes of non-static contact motions. Finally, the paper reports on experimental results that verify the theoretical predictions by using a 3-legged prototype.*

1 Introduction

Multi-legged robots performing quasistatic locomotion are becoming progressively more sophisticated. Developers of legged robots strive to achieve stable locomotion on uneven terrains such as staircases [20], traverse rough and hazardous terrain [1, 50], perform complex posture changes [60], climb along vertical pipes [38] or walls [7], and assist humans during planetary exploration [22, 57]. During quasistatic locomotion the mechanism moves through a continuum of equilibrium postures where it supports itself against gravity while moving its free limbs to new positions [3, 15, 28]. In order to achieve autonomous locomotion and explicit motion planning over uneven terrains [9, 24], one needs basic tools for characterizing postures that can passively support the mechanism against gravity. Under the assumption that the mechanism is supported by point contacts with Coulomb friction, three is the minimum number of supports that allow *quasistatic* locomotion over general uneven terrains in three dimensions. This paper focuses on 3-legged frictional equilibrium postures in a three-dimensional gravitational environment.

*Corresponding author: Dept. of ME, Technion, Haifa, Israel 32000, rimon@tx.technion.ac.il.

In order to characterize the feasible equilibrium postures, we first lump the complex kinematic structure of the mechanism into a single rigid body $\mathcal{B}$ having the same contacts with the environment and a variable center of mass. The feasible equilibrium postures associated with a given set of contacts correspond to center-of-mass locations that guarantee existence of contact reaction forces resulting in static equilibrium of $\mathcal{B}$. Under this reduction, our objective is as follows. Given a 3-contact arrangement of $\mathcal{B}$, we wish to identify the exact *feasible equilibrium region,* defined as all center-of-mass locations of $\mathcal{B}$ at which the contact forces can balance the gravitational wrench (i.e. force and torque) acting at $\mathcal{B}$'s center of mass. It is important to note here that this notion only gives a *necessary* condition for static equilibrium, since the existence of a static equilibrium solution for the rigid body does not necessarily imply that it will occur physically for the legged robot, which has to satisfy additional constraints, such as joint torque limitations [11]. Moreover, existence of static equilibrium must be augmented by analysis of the *dynamics* of the robot under contacts, which is beyond the scope of this paper. A brief discussion on these extensions appears in the concluding section.

Relationship to prior work. Static equilibrium postures (also termed *static stability*) received considerable attention in the early multi-legged locomotion literature [29, 34]. More recent papers discuss static stability of postures in the humanoid robots literature [20, 60]. When considering static stability of legged robots, a leading concept is the *support polygon principle* [34, 35]. It states that on a flat horizontal terrain, the mechanism's center-of mass must lie in the right prism whose cross section is the convex polygon spanned by the contacts. This principle was extended for dynamic motion synthesis of legged robots [23, 53] with the concept of *zero moment point* (ZMP) [54, 59], which states that in order to maintain contact during dynamic motion of the robot, the net wrench generated by gravitational and inertial forces must be a force having a line of action whose intersection point with the terrain lies within the support polygon. However, both the support polygon and the ZMP principles apply only to *flat horizontal terrains*, although extension of the ZMP principle to uneven terrains is under investigation [37, 47]. In the context of uneven terrains, the center-of-mass equilibrium region was characterized for *frictionless terrain* in [32], and is characterized for frictional contacts in *planar* environments in [42]. The latter paper also contains a preliminary result that the feasible equilibrium region in three-dimensions is an *infinite right cylinder* (i.e. a collection of infinite vertical lines) with a convex cross-section.

One expects that the grasping literature would provide valuable insights for the problem discussed in this paper. However, typical grasping systems differ from multi-legged mechanisms in three fundamental ways. First, the condition of *force closure* in grasping systems captures the fingers' ability to resist any external wrench acting on the grasped object [25, 39, 58]. In contrast, multi-legged mechanisms typically establish postures which are not in force closure, where the contact forces can only balance a subspace of external wrenches [21]. Second, grasping systems typically assume full control of the contact forces [13, 51], whereas in our case the contact forces are generated *passively*, and no active force control is assumed. In that sense, the postures considered here are most closely related to passive whole arm manipulation[1] [36, 40, 46] and fixturing applications [55, 61]. Third, in grasping applications the grasped object is typically an immobile rigid body or a passive

[1]In this application an object is manipulated by one or more articulated mechanisms which are allowed to establish multiple mid-link contacts with the manipulated object [2].

kinematic chain [8]. In contrast, a multi-legged mechanism can move its center-of-mass position and thus control the gravitational wrench. This situation is analogous to applications of *quasistatic manipulation*, where an object is actively pushed by multiple frictional contacts [12, 27], and its center-of-mass is moved in a way that ensures balancing of the gravitational wrench.

The grasping literature provides two computational approaches relevant to the problem considered here. The first approach approximates the quadratic friction cones in 3D by polyhedral cones [48], while the second approach formulates the frictional equilibrium constraints as a linear matrix inequality (LMI) problem [17]. In the context of quasistatic locomotion, computing the center-of-mass feasible equilibrium region then reduces to finding the projection of a high-dimensional convex cone to a two-dimensional plane [6]. Since the exact computation of this projection is highly complicated, Bretl and Lall [5, 6] proposed two methods for computating polygonal outer and inner approximations of this projection which are refined iteratively. In [5], they use polyhedral approximations of the friction cones to compute these polygons by solving a series of linear programs. In [6], they solve a series of convex optimization problems that account for the exact frictional constraints. These works were recently utilized in [4, 19] for development of motion planning algorithms for quasistatic legged locomotion, based on *probabilistic roadmaps* that sample discrete points of the robot's high-dimensional configuration space. However, even though [5] and [6] provide efficient procedures for computing the feasible equilibrium region for multiple frictional contacts on general uneven terrain, they do not provide any geometric or physical characterization of the boundary of this region. Focusing on a generic subclass of 3-contact arrangements, this paper complements these computational approaches with an analytic characterization of three different parts of the boundary, as well their association to the onset of different modes of non-static contact motion.

The paper makes the following contributions. First, it relates the feasible equilibrium region with the classical *support polygon* principle. The main result is identification a generic subclass of 3-contact arrangements called *tame*, and showing that for tame 3-contact arrangements, the feasible equilibrium region is bounded by the right prism spanned by the support polygon. Second, the paper provides a geometric and analytic characterization of the boundary of the feasible equilibrium region associated with tame 3-contact arrangements. The main result here is that the boundary curves are of three types, where two of them are linear segments which are obtained in a closed form, and the third is a highly nonlinear curve which is given implicitly as a solution of a set of nonlinear equations. Third, the paper provides physical insight into the boundary of the feasible equilibrium region by associating each type of boundary curve with the onset of a different mode of non-static motion at the contacts. Last, the paper uses a 3-legged prototype in order to experimentally verify the feasible equilibrium region and the onset of non-static motions associated with the three types of its boundary curves.

The structure of the paper is as follows. The next section introduces the terminology, defines the feasible equilibrium region, denoted $\mathcal{R}$, and reviews some of its basic properties. Section 3 defines the notion of tame 3-contact arrangements and relates the classical support polygon to the region $\mathcal{R}$ for these contact arrangements. Section 4 contains the main contribution of the paper—a geometric and analytic characterization of the three types of curves on the boundary of $\mathcal{R}$, and their association with different non-static contact modes. Section 5 present experimental verification of $\mathcal{R}$. The closing section discusses the feasible

x_i	: position of the i^{th} contact point
f_i	: the i^{th} contact force
$\boldsymbol{n}_i$	: unit vector normal to the i^{th} contact
$\boldsymbol{s}_i, \boldsymbol{t}_i$	: unit vectors such that $\{\boldsymbol{s}_i, \boldsymbol{t}_i, \boldsymbol{n}_i\}$ is a right-handed orthonormal frame
μ	: coefficient of static friction
C_i	: the i^{th} friction cone
$\mathsf{bdy}(\cdot)$	: denotes the boundary of a set
$\mathsf{int}(\cdot)$	: denotes the interior of a set
$\mathcal{B}$	: a rigid body representing the legged mechanism
$\boldsymbol{x}$	: position of the center-of-mass of $\mathcal{B}$
$\mathcal{R}$	: feasible equilibrium region of $\boldsymbol{x}$ positions
$\boldsymbol{e}$	: unit vector in the upward vertical direction
f_g	: gravitational force, directed along $-\boldsymbol{e}$
E	: matrix of projection onto horizontal plane
$\tilde{x}_i, \tilde{f}_i, \tilde{C}_i, \tilde{\boldsymbol{x}}, \widetilde{\mathcal{R}}$	: horizontal projections of $x_i, f_i, C_i, \boldsymbol{x}, \mathcal{R}$
Δ	: a plane that passes through x_1, x_2 and x_3
$\boldsymbol{\nu}$	: a unit vector normal to Δ

Table 1: Glossary of terms

equilibrium region associated with a higher number of contacts, as well as several future research directions. Finally, an appendix contains technical details and proofs of intermediate results.

2 Problem Statement

This section formulates the problem, defines the feasible equilibrium region for k-contact arrangements and reviews some of its basic properties. For the sake of clarity, Table 1 gives a glossary of the main terms used throughout this paper.

Let a 3D object $\mathcal{B}$ be supported by k frictional point contacts $x_1 \dots x_k$ against gravity. Let $f_1 \dots f_k$ be the contact reaction forces. We assume *hard-finger contacts* which generate negligible torque about the contact normals [30]. Let $\boldsymbol{x}$ denote the position of $\mathcal{B}$'s center-of-mass, and let f_g denote the gravitational force acting at $\boldsymbol{x}$. The static equilibrium condition of a given k-contact arrangement is

$$\sum_{i=1}^{k} \begin{pmatrix} f_i \\ x_i \times f_i \end{pmatrix} = - \begin{pmatrix} f_g \\ \boldsymbol{x} \times f_g \end{pmatrix}. \tag{1}$$

For a given set of $k \geq 3$ contacts and center-of-mass position $\boldsymbol{x}$, the solution for $f_1 \dots f_k$ in (1) is generically a $(3k-6)$-dimensional affine space in $\mathbb{R}^{3k}$. Under Coulomb's friction model the contact forces must additionally lie in their respective *friction cones*. The i^{th} friction cone is denoted C_i and is given by

$$C_i = \left\{ f_i : f_i \cdot \boldsymbol{n}_i \geq 0 \text{ and } (f_i \cdot \boldsymbol{s}_i)^2 + (f_i \cdot \boldsymbol{t}_i)^2 \leq (\mu f_i \cdot \boldsymbol{n}_i)^2 \right\}, \tag{2}$$

where μ is the coefficient of friction, $\boldsymbol{n}_i$ is the outward unit normal at x_i, and $(\boldsymbol{s}_i, \boldsymbol{t}_i)$ are unit tangents at x_i such that $\{\boldsymbol{s}_i, \boldsymbol{t}_i, \boldsymbol{n}_i\}$ is a right-handed orthonormal frame.

Assuming that the coefficient of friction and the contacts arrangement are given, the feasible equilibrium region of center-of-mass locations is defined as follows.

Definition 1. *For a given arrangement of contacts* $\{x_1 \dots x_k\}$*, contact normals* $\{\boldsymbol{n}_1 \dots \boldsymbol{n}_k\}$*, and a coefficient of friction* μ*, the* **feasible equilibrium region***, denoted* $\mathcal{R}$*, is the region of all possible center-of-mass locations* $\boldsymbol{x}$ *for which there exist contact reaction forces* $f_i \in C_i$ *(*$i = 1 \dots k$*) satisfying the static equilibrium condition (1).*

The goal of this paper is to characterize the feasible equilibrium region $\mathcal{R}$ for 3-contact arrangements. As a first step, we review some basic properties of this region, which were derived in [42].

Proposition 2.1 ([42])**.** *Let a 3D object* $\mathcal{B}$ *be supported by* k *frictional contacts against gravity in three-dimensions. If the feasible equilibrium region* $\mathcal{R}$ *is nonempty, it is a vertical line for a single contact, a vertical strip for two contacts, and generically a three-dimensional* **right cylinder with convex cross-section** *for* $k \geq 3$ *contacts.*

It is worth noting that for a single contact $\mathcal{R}$ is a vertical line passing through the contact, and for two contacts it is a vertical strip in the plane passing through the contacts. For $k \geq 3$ contacts, a special case occurs when all contacts are aligned along a common spatial line. In this non-generic case $\mathcal{R}$ degenerates to a two-dimensional vertical strip embedded in the vertical plane passing through the contacts. Based on the proposition, the computation of $\mathcal{R}$ requires computation of its horizontal cross-section, denoted $\widetilde{\mathcal{R}}$, in $\mathbb{R}^2$. Since $k=3$ is the smallest number of contacts for which $\mathcal{R}$ is fully three-dimensional, this paper focuses on the computation of $\widetilde{\mathcal{R}}$ for 3-contact arrangements. The concluding section discusses extension to higher number of contacts.

Finally, we review a result from [42], which gives a simple geometric procedure for constructing the feasible equilibrium region for *two frictional contacts in two dimensions*. This result will prove useful in the ensuing analysis, since cases involving only two nonzero contact forces in 3D will require consideration of planar subproblems. In two dimensions, the reaction force at a contact x_i must lie within a friction cone which is a planar sector. Let C_i denote the i^{th} planar friction cone, emanating from the contact x_i in $\mathbb{R}^2$. Let C_i^- denote the negative reflection of C_i about x_i (i.e. having negative normal component along $\boldsymbol{n}_i$). For simplicity, we assume that the friction cones are *upward pointing*, in the sense that $f_i \cdot \boldsymbol{e} > 0$ for all $f_i \in C_i$, $i = 1, 2$. For a given two-contact arrangement, let Π^{++} denote the infinite vertical strip spanned by the polygon $C_1 \cap C_2$. Similarly, let Π^{+-}, Π^{-+}, Π^{--} denote the infinite vertical strips spanned by the polygons $C_1 \cap C_2^-$, $C_1^- \cap C_2$, and $C_1^- \cap C_2^-$. Note that some of these polygons and their associated strips may be empty. Finally, let Π denote the infinite vertical strip bounded by the contacts x_1 and x_2. The following proposition uses the notation defined above to give a concrete formula for the feasible equilibrium region associated with two frictional upward pointing contacts in two-dimensions.

Proposition 2.2 ([42])**.** *Let* $\mathcal{B}$ *be supported by two frictional upward pointing contacts in a two-dimensional gravitational field. Then the feasible equilibrium region* $\mathcal{R}$ *is the infinite vertical strip given by*

$$\mathcal{R} = \big((\Pi^{++} \cup \Pi^{--}) \cap \Pi\big) \cup \big((\Pi^{+-} \cup \Pi^{-+}) \cap \overline{\Pi}\big), \tag{3}$$

where $\overline{\Pi}$ *is the complement of* Π *in* $\mathbb{R}^2$*.*

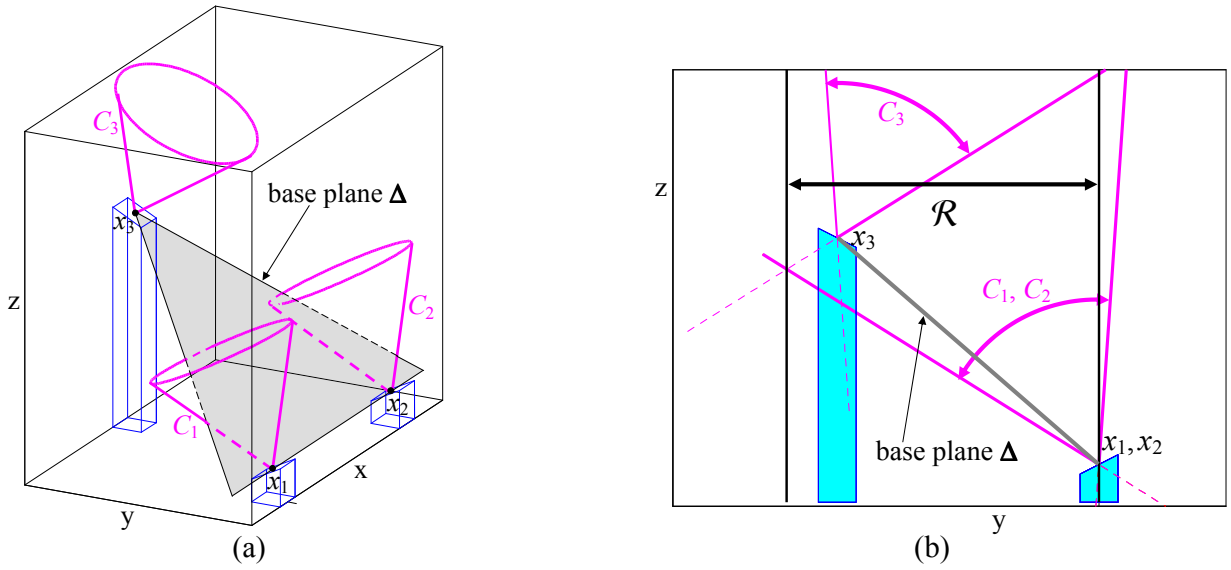

Figure 1: (a) A non-tame 3-contact arrangement, and (b) its projection onto yz plane.

3 Relation of $\mathcal{R}$ to Support Polygon

The classical *support polygon principle* (known as the tripod rule in 3-legged postures) is a simple criterion that determines the feasible equilibrium region on flat horizontal terrains [34], as follows. Define $E = \begin{bmatrix} 0 & -1 & 0 \\ 1 & 0 & 0 \end{bmatrix}$, which is a matrix that projects vectors in $\mathbb{R}^3$ onto their horizontal components in $\mathbb{R}^2$. Let $\tilde{x}_i = Ex_i$ denote the horizontal projection of the i^{th} contact point. The support polygon, deonted $\widetilde{\mathcal{P}}$, is then defined as the convex polygon spanned by $\{\tilde{x}_1 \dots \tilde{x}_k\}$ in $\mathbb{R}^2$, where in the 3-contact case, $\widetilde{\mathcal{P}}$ is simply a triangle. The right prism in $\mathbb{R}^3$ whose horizontal cross-section is $\widetilde{\mathcal{P}}$ is denoted $\mathcal{P}$. On general uneven terrain, the feasible equilibrium region $\mathcal{R}$ has no obvious relation to $\mathcal{P}$. This section introduces two classes of 3-contact arrangements that satisfy the relation $\mathcal{R} \subseteq \mathcal{P}$ or $\mathcal{P} \subseteq \mathcal{R}$. Focusing on contact arrangements satisfying $\mathcal{R} \subseteq \mathcal{P}$, we discuss a motivational example showing how $\mathcal{R}$ shrinks within $\mathcal{P}$ as the coefficient of friction decreases.

Let $\boldsymbol{e} = (0\ 0\ 1)$ denote the upward vertical direction. Let the *base plane*, denoted Δ, be the spatial plane passing through the three contacts. Let $\boldsymbol{\nu}$ denote the unit normal to Δ such that $\boldsymbol{e} \cdot \boldsymbol{\nu} \geq 0$. A contact x_i having a friction cone C_i is said to be *quasi-flat* if $\boldsymbol{e} \in C_i$. For example, in the contact arrangement of Figure 2(a) with $\mu = 0.7$, all contacts are quasi-flat. However, for the same contact arrangement with $\mu = 0.5$, x_3 is *not* quasi-flat, since the top view in Figure 2(b), showing the horizontal projection of the friction cone C_3, reveals that $\boldsymbol{e} \notin C_3$. The following generic subclass of 3-contact arrangements will be the focus of this paper.

Definition 2. *A 3-contact arrangement is* **tame** *if any nonzero force $f_i \in C_i$ satisfies $f_i \cdot \boldsymbol{\nu} > 0$ for $i = 1, 2, 3$.*

This means that the friction cones at the contacts lie strictly in the halfspace bounded by the base plane Δ and containing the upward direction $\boldsymbol{e}$. This definition captures the requirement that Δ would not be too steep with respect to $\boldsymbol{e}$. An example of a tame contact arrangement which is discussed below appears in Figure 2(a). An example of a non-tame

contact arrangement appears in Figure 1(a). The side view shown in Figure 1(b) reveals that the friction cone C_3 intersects the base plane Δ, thus violating the tame condition. A primary reason for focusing on tame contact arrangements is provided by the following proposition.

Proposition 3.1. *The feasible equilibrium region $\mathcal{R}$ of a* **tame 3-contact arrangement** *always lies within the right prism spanned by the support polygon, $\mathcal{R} \subseteq \mathcal{P}$. The converse relationship, $\mathcal{P} \subseteq \mathcal{R}$, always holds when all contacts are* **quasi-flat**.

A proof of the proposition appears in the Appendix. Note that a particular contact arrangement can be both tame and quasi-flat (e.g. on a gently undulating terrain with a sufficiently large coefficient of friction). In such cases $\mathcal{R} = \mathcal{P}$ (Figure 2(a)). The non-tame contact arrangement of Figure 1(a) is quasi-flat. This particular contact arrangement is symmetric with respect to a vertical plane passing through x_3. The cross-section of its region $\mathcal{R}$ through the symmetry plane can be computed with the methods derived in [42] for the two-dimensional case. The cross section, depicted in Figure 1(b), shows that $\mathcal{R}$ exceeds the support polygon. In contrast, for tame contact arrangements the region $\mathcal{R}$ always respects the support polygon as an outer boundary. Tame contact arrangements thus provide a natural middle-ground between flat horizontal terrains and vertical climbing scenarios. The remainder of this paper focuses on the characterization of the region $\mathcal{R}$ for tame 3-contact arrangements. The following example illustrates the challenge involved in this objective.

Motivational Example: Consider the 3-contact contact arrangement depicted in Figure 2(a). The contact arrangement is tame for $\mu \leq 0.7$, and we now consider its region $\widetilde{\mathcal{R}}$ for decreasing values of μ. Let $\tilde{x}_i$ and $\tilde{C}_i$ denote the horizontal projection of x_i and C_i. When $\mu = 0.7$ the contact arrangement is quasi-flat and $\widetilde{\mathcal{R}} = \widetilde{\mathcal{P}}$. When $\mu = 0.5$ the contacts x_1 and x_2 are still quasi-flat, hence $\tilde{x}_1$ and $\tilde{x}_2$ still lie in $\widetilde{\mathcal{R}}$. The convexity of $\widetilde{\mathcal{R}}$ implies that the entire line segment $\tilde{x}_1$–$\tilde{x}_2$ lies in $\widetilde{\mathcal{R}}$. Moreover, $\tilde{x}_1$–$\tilde{x}_2$ lies on the boundary of $\widetilde{\mathcal{R}}$, since it lies on the boundary of $\widetilde{\mathcal{P}}$ and $\widetilde{\mathcal{R}} \subseteq \widetilde{\mathcal{P}}$. However, the friction cone C_3 is no longer quasi-flat, as seen in top view in Figure 2(b). Now $\tilde{x}_3$ lies outside $\widetilde{\mathcal{R}}$ and only parts of the segments $\tilde{x}_1$–$\tilde{x}_3$ and $\tilde{x}_2$–$\tilde{x}_3$, ending at $\tilde{p}_1$ and $\tilde{p}_2$, lie on the boundary of $\widetilde{\mathcal{R}}$. Each of the line segments $\tilde{x}_i$–$\tilde{p}_i$ ($i = 1, 2$) is the horizontal projection of a vertical strip which is the feasible equilibrium region associated with two active contacts at x_3 and x_i. Note that the boundary of $\widetilde{\mathcal{R}}$ has an unknown missing piece between $\tilde{p}_1$ and $\tilde{p}_2$. Next consider the contact arrangement with $\mu = 0.4$, shown in Figure 2(c). Now $\tilde{C}_3$ does not contain $\tilde{x}_2$, and the contacts x_2 and x_3 alone cannot balance any gravitational load. Hence the segment $\tilde{x}_2$–$\tilde{x}_3$ lies outside $\widetilde{\mathcal{R}}$. The contacts x_1 and x_3 still contribute the segment $\tilde{x}_1$–$\tilde{p}_1$ to the boundary of $\widetilde{\mathcal{R}}$, but there is an unknown missing piece between $\tilde{p}_1$ and $\tilde{x}_2$. Finally, Figure 2(d) shows a top view of the friction cones for $\mu = 0.2$. Now only x_1 is quasi-flat. Since $\tilde{x}_1$ is still contained in $\tilde{C}_2$ and $\tilde{C}_3$, the boundary of $\widetilde{\mathcal{R}}$ consists of parts of the segments $\tilde{x}_1$–$\tilde{x}_2$ and $\tilde{x}_1$–$\tilde{x}_3$, ending at $\tilde{p}_2$ and $\tilde{p}_3$, together with an unknown piece connecting $\tilde{p}_2$ and $\tilde{p}_3$. Finally, when $\mu = 0.1$ (not shown in the figure), all three contacts are not quasi-flat, and $\widetilde{\mathcal{R}}$ lies strictly inside the support polygon.

The example illustrates the intricate structure of the region $\widetilde{\mathcal{R}}$ on uneven terrains. The example further illustrates that the support polygon provides the exact boundary of $\widetilde{\mathcal{R}}$ only when the contacts are all quasi-flat. On general tame 3-contact arrangements, a consideration of $\widetilde{\mathcal{P}}$ alone is unsafe, and our goal is to characterize the exact boundary of $\widetilde{\mathcal{R}}$ for these cases.

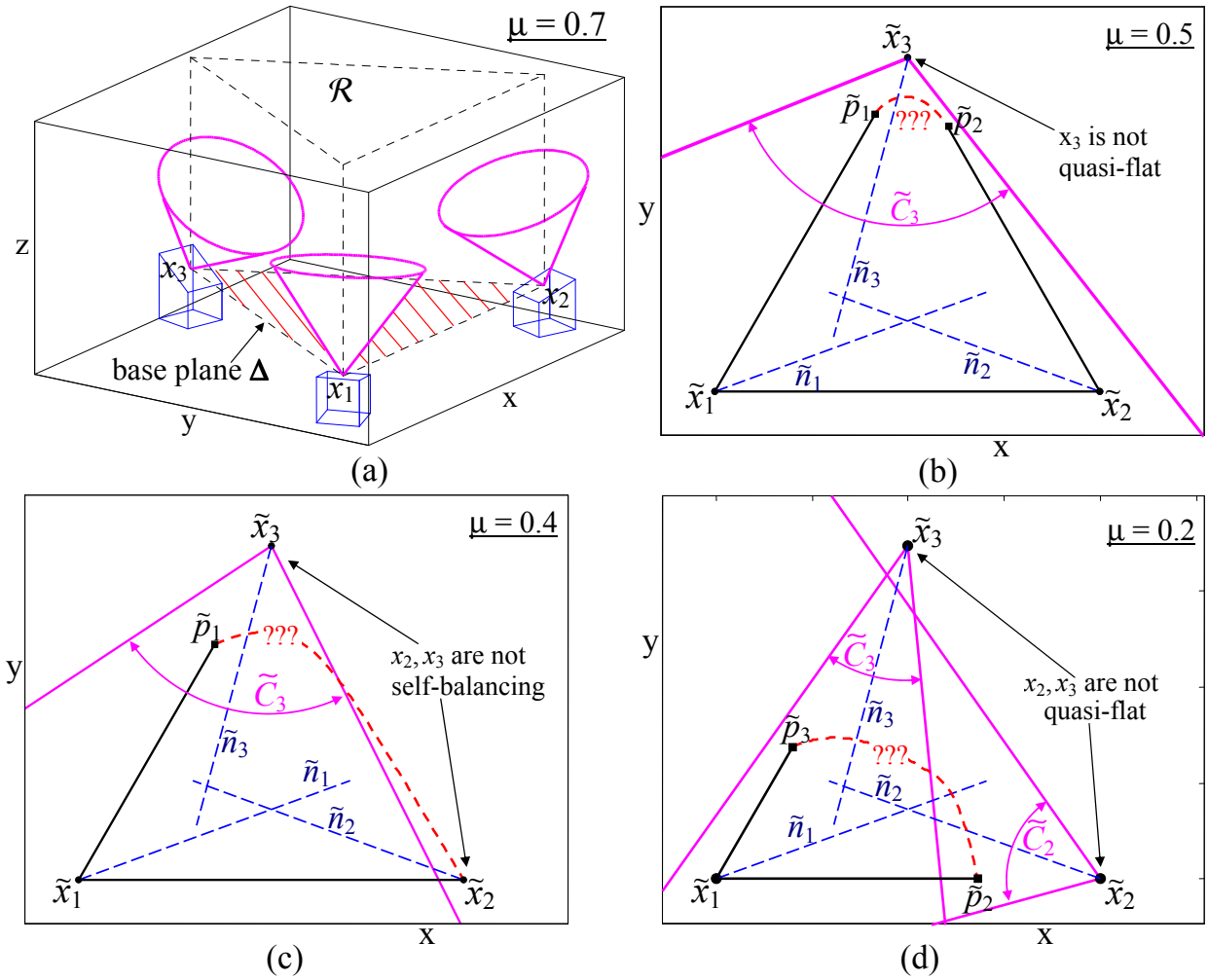

Figure 2: (a) A 3-contact contact arrangement which is tame and quasi-flat for $\mu = 0.7$. A top view of the contact arrangement for (b) $\mu = 0.5$, (c) $\mu = 0.4$, and (d) $\mu = 0.2$.

4 Analytic Characterization of Equilibrium Region $\mathcal{R}$

This section characterizes the boundary of the feasible equilibrium region for tame contact arrangements. First, we present the main result, which states that the boundary of $\widetilde{\mathcal{R}}$ consists of three types of boundary curves and gives geometric characterization and analytic expressions for each type. Next, we demonstrate the results via computation of the boundary of $\widetilde{\mathcal{R}}$ on a graphical example. Then we associate each type of boundary curve with the onset of a different non-static contact motion. Finally, we give the proof of the main result, where some of the technical details are relegated to the Appendix.

4.1 Main result

We now present the main result of this paper, which is a theorem that gives the full characterization of the boundary of $\widetilde{\mathcal{R}}$ for tame contact arrangements.

Preliminaries: As a setup for the theorem, we first establish some preliminary notation and definitions. First, observe that the static equilibrium condition (1) can be decomposed

into three sets of equations as

$$\begin{aligned} &a. \quad f_1 + f_2 + f_3 = \boldsymbol{e} \\ &b. \quad \boldsymbol{e} \cdot (x_1 \times f_1 + x_2 \times f_2 + x_3 \times f_3) = 0 \\ &c. \quad E(x_1 \times f_1 + x_2 \times f_2 + x_3 \times f_3) = E(\boldsymbol{x} \times \boldsymbol{e}), \end{aligned} \tag{4}$$

where the force units were scaled such that $\|f_g\| = 1$. Note that $\boldsymbol{x}$ appears only in part c in (4), which represents the horizontal components of the torque balance. Moreover, (4c) depends only on the horizontal projection of $\boldsymbol{x}$, defined as $\tilde{\boldsymbol{x}} = E\boldsymbol{x}$. It is easily shown that given contact forces (f_1, f_2, f_3), the horizontal projection $\tilde{\boldsymbol{x}}$ that satisfies (4c) is uniquely determined by the map

$$\tilde{\boldsymbol{x}} = \Psi(f_1, f_2, f_3), \text{ where } \Psi(f_1, f_2, f_3) = JE(x_1 \times f_1 + x_2 \times f_2 + x_3 \times f_3) \text{ and } J = \begin{bmatrix} 0 & -1 \\ 1 & 0 \end{bmatrix}. \tag{5}$$

Next, each friction cone C_i can be decomposed as $C_i = \{0\} \cup S_i \cup I_i$, where we denote $I_i = \mathsf{int}(C_i)$ and $S_i = \mathsf{bdy}(C_i) \setminus \{0\}$. A contact force $f_i \in S_i$ can be parametrized by the two scalars $(\lambda_i, \phi_i) \in I\!R^+ \times \mathbb{S}^1$, where λ_i is the force magnitude and ϕ_i the force angle, measured by projecting f_i on the plane spanned by $\{\boldsymbol{s}_i, \boldsymbol{t}_i\}$, which is terrain's tangent plane at the contact x_i. Using these parameters, a force $f_i \in S_i$ is given by

$$f_i(\lambda_i, \phi_i) = \lambda_i u_i(\phi_i) \quad \text{such that} \quad u_i(\phi_i) = \mu \cos(\phi_i)\boldsymbol{s}_i + \mu \sin(\phi_i)\boldsymbol{t}_i + \boldsymbol{n}_i \tag{6}$$

Since $u_i(\phi_i)$ has a fixed magnitude, $u_i'(\phi_i) = -\mu \sin(\phi_i)\boldsymbol{s}_i + \mu \cos(\phi_i)\boldsymbol{t}_i$ is orthogonal to $u_i(\phi_i)$. The pair $(u_i(\phi_i), u_i'(\phi_i))$ spans the *tangent plane* to S_i at $f_i(\lambda_i, \phi_i)$, which will be denoted by $\Delta_i(\phi_i)$. Finally, we define $\boldsymbol{\eta}_i(\phi_i) = u_i(\phi_i) \times u_i'(\phi_i) = -\mu \cos(\phi_i)\boldsymbol{s}_i - \mu \sin(\phi_i)\boldsymbol{t}_i - \mu^2 \boldsymbol{n}_i$, which is the outward-pointing normal to $\Delta_i(\phi_i)$ at $f_i(\lambda_i, \phi_i)$. With a slight abuse of notation, we will treat $\Delta_i(\phi_i)$ as planes embedded in the *physical space*, that is, planes which are tangent to the friction cones C_i emanating from the contact points x_i in the three-dimensional space.

Statement of the main theorem: Having defined all the necessary notation, we now present the main theorem, which formulates the three different types of curves comprising the boundary of $\widetilde{\mathcal{R}}$, where each type of boundary curve is associated with contact forces having a particular characterization. The first type of boundary curves are linear segments lying on edges of the support polygon $\widetilde{\mathcal{P}}$, which can be computed by applying the planar formula in Proposition 2.2 for two-dimensional environments. The two other curves are formulated as the image of one-dimensional curves in the space of contact forces (f_1, f_2, f_3) under the map Ψ defined in (5). For simplicity, each boundary curve is formulated under an arbitrary assignment of indices to the contacts and contact forces, and represents *three* different curves obtained by applying all possible permutations of index relabeling.

Theorem 1. *Given a tame* 3*-contact arrangement, the boundary of the horizontal cross-section* $\widetilde{\mathcal{R}}$ *of the feasible equilibrium region consists of three types of curves, which are listed as follows:*

1. **Two-contact segment** *is a linear segment lying on an edge* $\tilde{x}_1 - \tilde{x}_2$ *of the support polygon* $\widetilde{\mathcal{P}}$*, which is associated with contact forces* (f_1, f_2, f_3) *such that* $f_3 = 0$*. The endpoints of the line segments can be obtained by applying the planar formula given in*

Proposition 2.2 for computing $\mathcal{R}$ in two-dimensional environments, where the forces $f_1 \in C_1$ and $f_2 \in C_2$ are restricted to lie within the plane spanned by the vertical direction $\boldsymbol{e}$ and the line $\tilde{x}_1 - \tilde{x}_2$.

2. **Three-contact SSI segments** *are linear segments which are associated with contact forces such that $f_1 \in S_1$, $f_2 \in S_2$ and $f_3 \in I_3$. The forces f_1, f_2 are parametrized as $f_i = \lambda_1 u_i(\phi_i^*)$ for $i = 1, 2$, where ϕ_1^*, ϕ_2^* are solutions of the equations*

$$\begin{aligned} \boldsymbol{\eta}_i(\phi_1^*) \cdot (x_1 - x_3) &= 0 \\ \boldsymbol{\eta}_i(\phi_2^*) \cdot (x_2 - x_3) &= 0, \end{aligned} \tag{7}$$

that satisfy the additional sign condition

$$\mathsf{sgn}\big(\hat{l} \cdot ((x_1 - x_3) \times \boldsymbol{n}_1)\big) = \mathsf{sgn}\big(\hat{l} \cdot ((x_2 - x_3) \times \boldsymbol{n}_2)\big), \text{ where } \hat{l} = \boldsymbol{\eta}_1(\phi_1^*) \times \boldsymbol{\eta}_2(\phi_2^*). \tag{8}$$

The boundary curve is then given as the Ψ-image of the line in (f_1, f_2, f_3)-space which is obtained by solving the four scalar equations (4a)-(4b) with the five scalar unknowns λ_1, λ_2 and f_3, where ϕ_1^* and ϕ_2^* are solutions of (7) that also satisfy (8). The geometric meaning of (7) is that the tangent planes $\Delta_1(\phi_1^*)$ and $\Delta_2(\phi_2^*)$ pass through the contact x_3. The boundary curve of $\widetilde{\mathcal{R}}$ is a linear segment lying on the horizontal projection of l, the intersection line of the tangent planes $\Delta_1(\phi_1^*)$ and $\Delta_2(\phi_2^*)$.

3. **Three-contact SSS curve** *is associated with contact forces such that $f_i \in S_i$ for all $i = 1, 2, 3$. The forces are parametrized by λ_i, ϕ_i, where the angles (ϕ_1, ϕ_2, ϕ_3) lie on the one-dimensional solution set of the two equations*

$$\det \begin{bmatrix} Eu_1(\phi_1) & Eu_2(\phi_2) & Eu_3(\phi_3) \\ \boldsymbol{e} \cdot (x_1 \times u_1(\phi_1)) & \boldsymbol{e} \cdot (x_2 \times u_2(\phi_2)) & \boldsymbol{e} \cdot (x_3 \times u_3(\phi_3)) \end{bmatrix} = 0 \tag{9}$$

$$\det \begin{bmatrix} H^T(\boldsymbol{\nu} \times \boldsymbol{\eta}_1(\phi_1)) & H^T(\boldsymbol{\nu} \times \boldsymbol{\eta}_2(\phi_2)) & H^T(\boldsymbol{\nu} \times \boldsymbol{\eta}_3(\phi_3)) \\ \boldsymbol{\nu} \cdot (x_1 \times (\boldsymbol{\nu} \times \boldsymbol{\eta}_1(\phi_1))) & \boldsymbol{\nu} \cdot (x_2 \times (\boldsymbol{\nu} \times \boldsymbol{\eta}_2(\phi_2))) & \boldsymbol{\nu} \cdot (x_3 \times (\boldsymbol{\nu} \times \boldsymbol{\eta}_3(\phi_3))) \end{bmatrix} = 0 \tag{10}$$

where H is a 3×2 constant matrix whose columns form an orthogonal basis for the base plane Δ. Geometrically, (9) implies that the lines of the three contact forces intersect a common vertical line, and (10) implies that the intersection point of the three tangent planes $\Delta_1(\phi_1), \Delta_2(\phi_2), \Delta_3(\phi_3)$, denoted z, lies on the base plane Δ. Finally, an additional necessary condition for a triplet (ϕ_1, ϕ_2, ϕ_3) that solves (9)-(10) to contribute to the boundary of $\widetilde{\mathcal{R}}$ is the sign condition given by

$$\mathsf{sgn}\big(\boldsymbol{\nu} \cdot ((x_1 - z) \times \boldsymbol{\eta}_1(\phi_1))\big) = \mathsf{sgn}\big(\boldsymbol{\nu} \cdot ((x_2 - z) \times \boldsymbol{\eta}_2(\phi_2))\big) = \mathsf{sgn}\big(\boldsymbol{\nu} \cdot ((x_3 - z) \times \boldsymbol{\eta}_3(\phi_3))\big). \tag{11}$$

The boundary curve is then given as the Ψ-image of the one-dimensional curve in (f_1, f_2, f_3)-space which is obtained by taking $f_i = \lambda_i u_i(\phi_i)$ for $i = 1, 2, 3$ where λ_i are obtained by solving the linear equation (4b) for any value of (ϕ_1, ϕ_2, ϕ_3) that lies on the one-dimensional solution set of (9) and (10).

Practical computation of the SSS boundary curves: Note that while the first two types of boundary curves are linear segments which are given in closed form and have a straightforward geometric interpretation, the third type of boundary curve is only given *implicitly* as an image of the solution curve of two equations in (ϕ_1, ϕ_2, ϕ_3)-space, which are cubic in $(\cos\phi_i, \sin\phi_i)$. Two ways for practical numeric computation of these curves, which are both implemented in our graphical examples, are as follows. First, the trigonometric equations (9)-(10) can be transformed into polynomial equations by using the new variables $\beta_i = \tan(\phi_i/2)$. Then, β_3 can be eliminated, yielding a single polynomial equation of order 16 is β_1, β_2. This equation is then solved numerically by discretizing ϕ_1 within the interval $[-\pi, \pi]$ and finding the real roots of an 8th order polynomial in β_2 for any discrete value of β_1 (see [41] for details). A second way for computing SSS curves is to trace them numerically by differentiating (9)-(10) and marching along the tangent to the solution in (ϕ_1, ϕ_2, ϕ_3)-space. However, this approach requires pre-computation of sample points on each piece of the SSS curves. A practical approach for computing sample points is based on the following corollary.

Corollary 4.1. *The SSS curves along the boundary of $\widetilde{\mathcal{R}}$ are separated from each other by two-contact segments and three-contact SSI segments. When the boundary of $\widetilde{\mathcal{R}}$ consists only of SSS curves, it is the image of a single connected loop in (ϕ_1, ϕ_2, ϕ_3)-space.*

A proof sketch of this corollary appears in the Appendix. The corollary provides us with the following approach for computing sample points on the SSS curves along the boundary of $\widetilde{\mathcal{R}}$. First one computes all linear segments on the boundary of $\widetilde{\mathcal{R}}$ using the formulas provided in Theorem 1. Since $\widetilde{\mathcal{R}}$ is convex, its boundary is a simple closed curve. The remaining pieces on the boundary of $\widetilde{\mathcal{R}}$ must be SSS curves. The corollary guarantees that the endpoints of each SSS curve are endpoints of its neighboring linear segments. The (ϕ_1, ϕ_2, ϕ_3)-values of the latter endpoints provide start-and-end points for tracing the SSS curve joining the two linear segments. However, this approach ceases to be useful once the boundary of $\widetilde{\mathcal{R}}$ consists only of SSS curves. In this case the corollary guarantees that the boundary of $\widetilde{\mathcal{R}}$ originates from a *single connected loop* in (ϕ_1, ϕ_2, ϕ_3)-space. In this case a sample point on the boundary of $\widetilde{\mathcal{R}}$ can be efficiently computed as a convex optimization problem [5, 17]. This computation takes place in $(f_1, f_2, f_3, \tilde{\boldsymbol{x}})$-space and gives a starting point on the (ϕ_1, ϕ_2, ϕ_3)-loop generating the boundary of $\widetilde{\mathcal{R}}$.

4.2 Graphical Example

We now demonstrate the application of Theorem 1 for computing the boundary of $\widetilde{\mathcal{R}}$. Figure 3 shows the region $\widetilde{\mathcal{R}}$ (shaded region) for the 3-contact arrangement of Figure 2, using several values of μ. The boundary of $\widetilde{\mathcal{R}}$ consists of two-contact segments (thick lines), three-contact SSI segments (dashed lines), and three-contact SSS curves (solid curves). Figures 3(a)-(c) correspond to $\mu = 0.5, 0.4, 0.2$ and resolve the missing boundary pieces of $\widetilde{\mathcal{R}}$ in Figures 2(b)-(d) respectively. Figure 3(d) shows the region $\widetilde{\mathcal{R}}$ for a smaller value of $\mu = 0.1$. In this case $\widetilde{\mathcal{R}}$ lies strictly inside the support polygon $\widetilde{\mathcal{P}}$, and its boundary consists of one SSI segment and one SSS curve. Note that the region $\widetilde{\mathcal{R}}$ is convex for all values of μ.

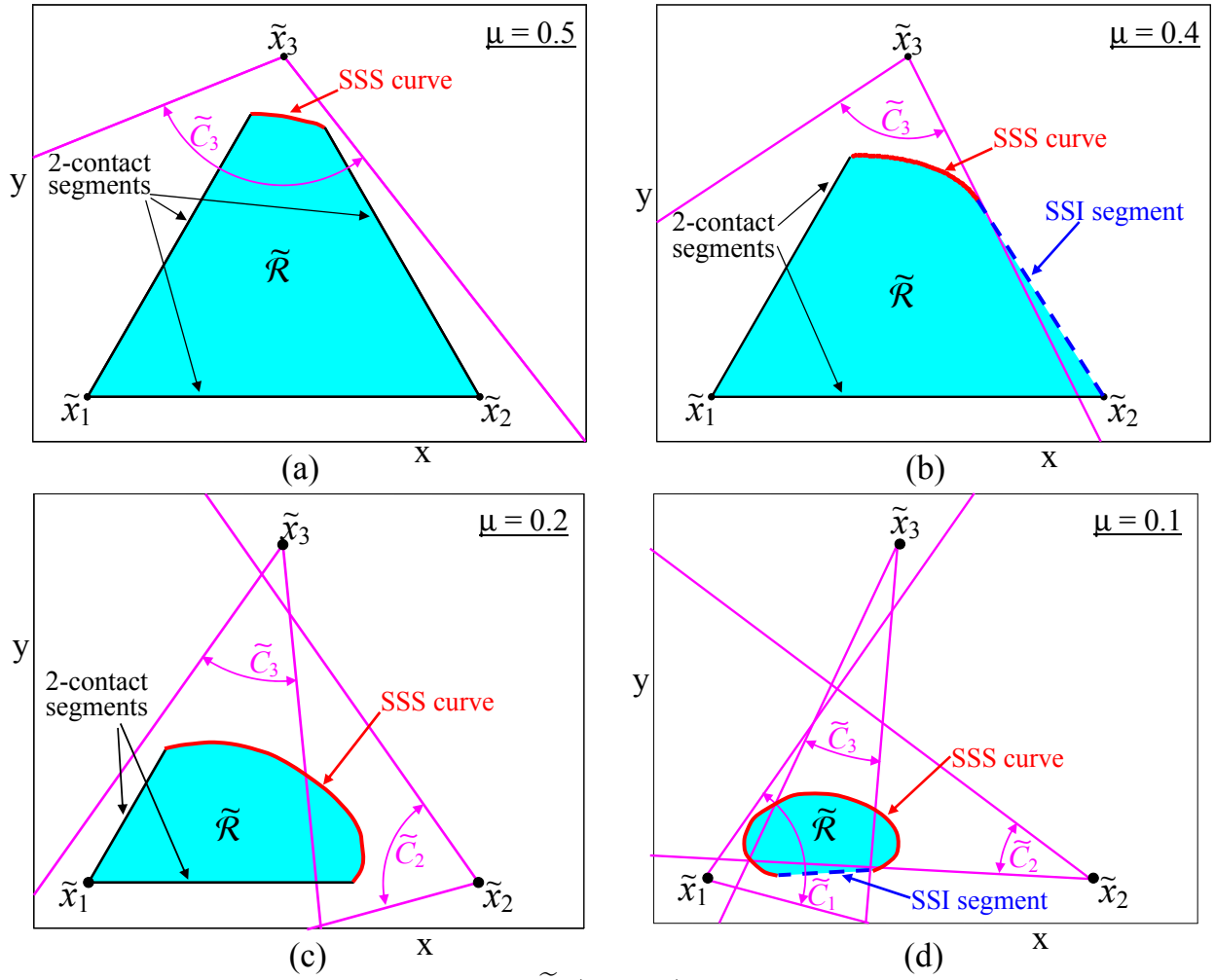

Figure 3: The horizontal cross section $\widetilde{\mathcal{R}}$ (shaded) for the tame 3-contact arrangement of Figure 2, using (a) $\mu = 0.5$, (b) $\mu = 0.4$, (c) $\mu = 0.2$, and (d) $\mu = 0.1$.

4.3 Onset of Non-Static Motion Modes

The boundary of $\widetilde{\mathcal{R}}$ consists of three types of curves listed in Theorem 1. When $\mathcal{B}$'s horizontal center-of-mass position crosses the boundary of $\widetilde{\mathcal{R}}$ into the non-equilibrium region, one expects that $\mathcal{B}$ would enter a non-static motion mode. The particular motion mode depends on the boundary curve being crossed. When $\tilde{\boldsymbol{x}}$ reaches a two-contact segment on a support-polygon edge, the contact forces lie in one of the closed cells $\{0\}\times C_2\times C_3$, $C_1\times\{0\}\times C_3$, $C_1\times C_2\times\{0\}$. These cells involve two active forces while the third force has zero magnitude. Hence one expects the onset of a tip-over motion, where the two active contacts start rolling while the non-active contact breaks away from the supporting terrain. When $\tilde{\boldsymbol{x}}$ reaches a two-contact SSI segment, the contact forces lie in one of the cells $\mathsf{int}(C_1)\times S_2\times S_3$, $S_1\times\mathsf{int}(C_2)\times S_3$, $S_1\times S_2\times\mathsf{int}(C_3)$. In these cells one force f_i lies in the interior of its friction cone, while the other two forces f_j, f_k lie on the boundary of their friction cones. Hence one expects the onset of a rolling motion at x_i, accompanied by simultaneous sliding at x_j and x_k. When $\tilde{\boldsymbol{x}}$ reaches an SSS curve the contact forces lie in $S_1\times S_2\times S_3$, and in this case one expects the onset of simultaneous sliding at all three contacts.

The three non-static modes match the experimental results reported below. However,

one should keep in mind that rigid-body dynamics with Coulomb friction at the contacts can exhibit multiple solutions as well as non-smooth transitions in the form of impacts [26, 56]. Current research efforts aimed at improving the predictive powers of the rigid-body dynamic model are discussed in the concluding section.

4.4 Proof of the Main Result

We now give the proof of Theorem 1. First, we give the idea of the proof and outline its main steps. Then we go through these steps by giving a series of intermediate statements whose detailed proofs are relegated to the Appendix.

Main idea of the proof. The proof is based on the following geometric interpretation of the equilibrium condition (1). Let *wrench space* have force-and-torque coordinates $(f, \tau) \in \mathbb{R}^6$. As the center of mass $\boldsymbol{x}$ varies in physical space, the gravitational wrench on the right side of (1) spans a two-dimensional affine subspace in wrench space (the component of $\boldsymbol{x}$ along $\boldsymbol{e}$ is mapped to zero). Let L denote this subspace. On the other hand, as the contact forces vary in their friction cones, their net reaction wrench on the left side of (1) spans a six-dimensional cone in wrench space. Let W denote this cone. For 3-contact arrangements, the intersection $W \cap L$ is generically a two-dimensional set, consisting of all feasible reaction wrenches which balance the gravitational wrench for some horizontal position of the center of mass $\tilde{\boldsymbol{x}}$. The wrenches $(f, \tau) \in W \cap L$ are related to $\boldsymbol{x}$ via the linear mapping $\tau = \boldsymbol{x} \times f_g$. Hence we first compute the boundary of $W \cap L$ in wrench space, then obtain the boundary of $\mathcal{R}$ by inversion of the linear relation $\tau = \boldsymbol{x} \times f_g$, as given by the map Ψ in (5).

The computation of the boundary of $\mathcal{R}$ is thus divided into three stages. First, we characterize and formulate the boundary of the six-dimensional wrench cone W. We show that this boundary is composed of three different types of cells. Each boundary cell is a five-dimensional set of wrenches generated by *critical contact forces* having a distinct parametrization and a particular geometric characterization. Next, we intersect each boundary cell of W with the two-dimensional affine subspace L. This is done by taking the contact-force parametrization and augmenting it with the linear system of four scalar equations in (4a)-(4b), yielding a parametrization of the one-dimensional boundary curve of $W \cap L$. Finally, the boundary of $\widetilde{\mathcal{R}}$ is the pre-image of $\mathsf{bdy}(W) \cap L$ under the linear map $\tau = \boldsymbol{x} \times f_g$, which is obtained by applying the explicit map Ψ given in (5). In the rest of this section, we go over these stages, where the main focus is on the details of the first stage, namely, computation of the boundary of the wrench cone W.

Stage 1: Computing the boundary of the wrench cone W. We now characterize the critical contact forces whose net wrench lies on the boundary of W. By definition, W is the collection of net wrenches generated by varying the contact forces within their friction cones,

$$W = \left\{ \sum_{i=1}^{3} \begin{pmatrix} f_i \\ x_i \times f_i \end{pmatrix} \,:\, f_i \in C_i \text{ for } i = 1, 2, 3 \right\}, \tag{12}$$

where the requirement $f_i \in C_i$ for $i = 1, 2, 3$ is equivalent to $(f_1, f_2, f_3) \in C_1 \times C_2 \times C_3$. The boundary of W is generically a five-dimensional set in wrench space $\mathbb{R}^6$. In order to characterize this set, we interpret W as the image of $C_1 \times C_2 \times C_3 \subset \mathbb{R}^9$ under a linear mapping $\mathcal{L}$ given by

$$\mathcal{L} : C_1 \times C_2 \times C_3 \to I\!R^6 \quad \text{where} \quad \mathcal{L}(f_1, f_2, f_3) = \sum_{i=1}^{3} \begin{pmatrix} f_i \\ x_i \times f_i \end{pmatrix}. \tag{13}$$

It can be verified that $\mathcal{L}$ has full rank whenever the three contacts do not lie along a common spatial line. Assuming that $\mathcal{L}$ has full rank, the inverse function theorem [16, p. 20] implies that $\mathcal{L}$ maps the interior of $C_1 \times C_2 \times C_3$ into the interior of W. Hence the boundary of W is generated by contact forces on the boundary of $C_1 \times C_2 \times C_3$. The boundary of $C_1 \times C_2 \times C_3$ is an eight-dimensional set given by the union: $\mathsf{bdy}(C_1 \times C_2 \times C_3) = \mathsf{bdy}(C_1) \times C_2 \times C_3 \cup C_1 \times \mathsf{bdy}(C_2) \times C_3 \cup C_1 \times C_2 \times \mathsf{bdy}(C_3)$. For notational simplicity we focus on the set $\mathsf{bdy}(C_1) \times C_2 \times C_3$, with the understanding that similar results apply to the other two sets. We need to obtain the internal division of $\mathsf{bdy}(C_1) \times C_2 \times C_3$ into cells[2], then determine which cells contribute to the boundary of W. Recall that S_i denotes the boundary of the i^{th} friction cone C_i, excluding its vertex. The following lemma lists the cells of $\mathsf{bdy}(C_1) \times C_2 \times C_3$.

Lemma 4.2. *The set* $\mathsf{bdy}(C_1) \times C_2 \times C_3$ *consists of force-cells of different dimensions, which are listed as:*

1. $\{0\} \times S_2 \times \mathsf{int}(C_3)$, $\{0\} \times \mathsf{int}(C_2) \times S_3$, $S_1 \times \mathsf{int}(C_2) \times \{0\}$, $S_1 \times \{0\} \times \mathsf{int}(C_3)$ (four 5D cells),
2. $\{0\} \times \mathsf{int}(C_2) \times \mathsf{int}(C_3)$ (one 6D cell),
3. $S_1 \times S_2 \times S_3$ (one 6D cell),
4. $S_1 \times S_2 \times \mathsf{int}(C_3)$ *and* $S_1 \times \mathsf{int}(C_2) \times S_3$ (two 7D cells),
5. $S_1 \times \mathsf{int}(C_2) \times \mathsf{int}(C_3)$ (one 8D cell),

where the list includes only cells of dimension five and higher.

A proof of the lemma appears in the Appendix. Our next task is to determine which of the force-cells listed in the lemma contribute five-dimensional pieces to the boundary of W. First, we parametrize each force-cell of dimension m by a set of m scalar parameters, where an interior force $f_i \in I_i$ is parametrized by its three components in $I\!R^3$, and a force on the boundary of its friction cone $f_i \in S_i$ is parametrized by $(\lambda_i, \phi_i) \in I\!R^+ \times I\!R$ as defined in (6). The restriction of the map $\mathcal{L}$ to the cell can then be obtained by substituting the chosen parametrization of contact forces into (13). Then, a necessary condition that the image of the force-cell under $\mathcal{L}$ would contribute to the boundary of W is that *the Jacobian of the restriction of* $\mathcal{L}$ *to the cell would lose its rank.* For each m-dimensional cell, the corresponding Jacobian matrix has dimensions of $6 \times m$, and the condition for rank-deficiency gives $m - 5$ equations that determine the *critical contact forces* belonging to the particular force-cell. These conditions are given a geometric interpretation which is proven in the Appendix by using the theory of *line geometry* [10, 33]. In line geometry, a vector of the form $(v, p \times v) \in I\!R^6$ is interpreted as a representation of a spatial line in $I\!R^3$, and the linear dependency of a set of such vectors implies particular geometric relations between their corresponding lines. The following proposition specifies which of the force-cells listed in Lemma 4.2 possibly contribute to the boundary of W, and gives analytic expressions and geometric characterization of the corresponding critical forces. The geometric characterization makes use of the tangent planes $\Delta_i(\phi_i)$, which were defined for $f_i \in S_i$, and their relations to the contact points and the base plane Δ.

[2]Each *cell* being an m-dimensional manifold without a boundary, where $0 \leq m \leq 8$.

Proposition 4.3. *Let x_1, x_2, x_3 be three contacts which do not lie on a common spatial line. Among the force-cells listed in Lemma 4.2, the ones listed as items 1-4 possibly contribute five-dimensional pieces to the boundary of the wrench cone W, where the critical contact forces are given as follows*

1. **Two-contact cells:** *the entire 5D cells.*

2. **Two-contact cells:** *the entire 6D cell $\{0\}\times\mathsf{int}(C_2)\times\mathsf{int}(C_3)$.*

3. **SSS cells:** *the subset of the 6D cell $S_1\times S_2\times S_3$ of forces (f_1, f_2, f_3) whose tangent planes $\Delta_i(\phi_i)$ intersect at a common point z on the base plane Δ. The forces are parametrized by (λ_i, ϕ_i) such that (ϕ_1, ϕ_2, ϕ_3) satisfy the relation (10).*

4. **SSI cells:** *The subset of the 7D cell $S_1\times S_2\times\mathsf{int}(C_3)$ having forces (f_1, f_2) whose tangent planes $\Delta_1(\phi_1)$ and $\Delta_2(\phi_2)$ intersect at x_3. These forces are given by $f_1 = \lambda_1 u_1(\phi_1^*)$ and $f_2 = \lambda_2 u_2(\phi_2^*)$ where ϕ_1^*, ϕ_2^* are solutions of (7), and λ_1, λ_2 and $f_3 \in \mathsf{int}(C_3)$ vary freely. The subset of the force-cell $S_1\times\mathsf{int}(C_2)\times S_3$ is similarly defined.*

5. The 8D cell of item 5 generically does not contribute to the boundary of W.

The proof of this proposition appears in the Appendix. Note that the force-cells of items 1 and 2 involve only two nonzero contact forces, while the force-cells of items 3 and 4 involve three nonzero contact forces. Also note that the subset of the 7D force-cell $S_1\times S_2\times\mathsf{int}(C_3)$ involves four combinations of forces (f_1, f_2) with fixed directions, while $f_3 \in \mathsf{int}(C_3)$.

An important observation is that for each force-cell, the condition of rank-deficiency of the Jacobian which describes the critical contact forces is only a *necessary* condition for characterization of wrenches on the boundary of W. That is, the critical contact forces described in Proposition 4.3 are mapped to *candidate* boundary cells of W, where some of the candidate boundary cells might actually lie in the *interior* of W. (As a simple analogy from single-variable calculus, the rank-deficiency condition is equivalent to the vanishing of the first derivative of a scalar function, which indicates a local critical point. In order to determine whether the critical point corresponds to a minimum, one is required to check some additional sign conditions). The following proposition completes the characterization of $\mathsf{bdy}(W)$ by augmenting the conditions in Proposition 4.3 with *sufficient* conditions for critical contact forces to be associated with the *actual boundary* of W rather than its interior. The conditions utilize the geometric characterization of the critical forces, the convexity of W, and the fact that we focus on tame contact arrangements.

Proposition 4.4. *Given a tame 3-contact arrangement, consider the characterization of critical contact forces as given in Proposition 4.3. The sufficient conditions for critical forces from each force-cell to contribute to the actual boundary of the wrench cone W are given as follows*

1. **Two-contact cells:** *the entire 5D cells map to the actual boundary of W.*

2. **Two-contact cells:** *the entire 6D cell $\{0\}\times\mathsf{int}(C_2)\times\mathsf{int}(C_3)$ maps to the actual boundary of W.*

3. **SSS cells:** *from the subset of the 6D cell $S_1\times S_2\times S_3$ associated with critical forces (f_1, f_2, f_3) whose tangent planes $\Delta_i(\phi_i)$ intersect at a common point z on the base plane Δ, the critical forces which contribute to the actual boundary of W must satisfy the additional condition*

$$\mathsf{sgn}\big(\boldsymbol{\nu}\cdot((x_1-z)\times\boldsymbol{\eta}_1(\phi_1))\big) = \mathsf{sgn}\big(\boldsymbol{\nu}\cdot((x_2-z)\times\boldsymbol{\eta}_2(\phi_2))\big) = \mathsf{sgn}\big(\boldsymbol{\nu}\cdot((x_3-z)\times\boldsymbol{\eta}_3(\phi_3))\big).$$

4. **SSI cells:** *from the subset of the 7D cell $S_1 \times S_2 \times \mathsf{int}(C_3)$ associated with critical forces $f_1 = \lambda_1 u_1(\phi_1^*)$ and $f_2 = \lambda_2 u_2(\phi_2^*)$, the critical forces which contribute to the actual boundary of W must satisfy the additional condition*

$$\mathsf{sgn}\big(\hat{l}\cdot((x_1 - x_3) \times \boldsymbol{n}_1)\big) = \mathsf{sgn}\big(\hat{l}\cdot((x_2 - x_3) \times \boldsymbol{n}_2)\big), \text{ where } \hat{l} = \boldsymbol{\eta}_1(\phi_1^*) \times \boldsymbol{\eta}_2(\phi_2^*).$$

A proof of this proposition appears in the Appendix.

Stages 2 and 3: Computing the boundary curves of $\widetilde{\mathcal{R}}$. The five-dimensional boundary cells of the wrench cone W were characterized and formulated in Propositions 4.3 and 4.4. We now proceed to the next two stages of intersecting $\mathsf{bdy}(W)$ with the affine subspace L in wrench space to obtain $\mathsf{bdy}(W \cap L)$, and then applying the map Ψ in (5) to obtain a formulation of the three pieces of curves comprising the boundary $\mathsf{bdy}(\widetilde{\mathcal{R}})$. The first type of boundary curves, namely, the two-contact segments, associated with two nonzero contact forces f_i and f_j are computed directly by applying the planar formula in Proposition 2.2 for computing the planar strip of feasible equilibrium in two dimensional environments, where the forces f_i and f_j are restricted lie within the plane spanned by the vertical direction $\boldsymbol{e}$ and the line $x_i - x_j$. The resulting strip has a vertical projection lying on the edge $\tilde{x}_i - \tilde{x}_j$ of the support polygon, which is precisely a two-contact segment on $\mathsf{bdy}(\widetilde{\mathcal{R}})$. Note that proposition 3.1 implies that for tame contact arrangement, any non-empty two-contact segment is automatically on the boundary of $\widetilde{\mathcal{R}}$. For the second type of cells of $\mathsf{bdy}(W)$, namely, SSI cell, the corresponding linear segment on the boundary of $\widetilde{\mathcal{R}}$ is obtained by solving the four scalar equations (4a)-(4b) with the five scalar unknowns λ_1, λ_2 and f_3, to obtain a line segment in (f_1, f_2, f_3)-space, then applying the linear map Ψ to yield the line segment on $\mathsf{bdy}(\widetilde{\mathcal{R}})$. This line segment can be given the following geometric interpretation. Recall that ϕ_1^* and ϕ_2^* are chosen such that the line of intersection of the two tangent planes $\Delta_1(\phi_1^*)$ and $\Delta_2(\phi_2^*)$, denoted l, passes through x_3. By construction, the action lines of all three contact forces intersect l, and hence they generate zero torque about this line. Since the gravitational force acting at $\boldsymbol{x}$ must also generate zero torque about l in order to achieve torque balance, we conclude that the corresponding SSI line segment on $\mathsf{bdy}(\widetilde{\mathcal{R}})$ must be the horizontal projection of l. Finally, for the third type of cell of $\mathsf{bdy}(W)$, namely, SSS cells, the critical contact forces are given by $f_i = \lambda_i u_i(\phi_i)$ for $i = 1, 2, 3$, where (ϕ_1, ϕ_2, ϕ_3) satisfy the relation (10). In order to intersect with the affine subspace L, one needs to substitute the forces f_i into (4a)-(4b). Augmenting only the (x, y)-components of the force balance (4a) with the torque balance about $\boldsymbol{e}$ in (4b), one obtains

$$\begin{pmatrix} Ef_1 \\ \boldsymbol{e}\cdot(x_1 \times f_1) \end{pmatrix} + \begin{pmatrix} Ef_2 \\ \boldsymbol{e}\cdot(x_2 \times f_2) \end{pmatrix} + \begin{pmatrix} Ef_3 \\ \boldsymbol{e}\cdot(x_3 \times f_3) \end{pmatrix} = \begin{pmatrix} 0 \\ 0 \\ 0 \end{pmatrix}.$$

Substituting $f_i = \lambda_i u_i(\phi_i)$ gives:

$$\begin{bmatrix} Eu_1(\phi_1) & Eu_2(\phi_2) & Eu_3(\phi_3) \\ \boldsymbol{e}\cdot(x_1 \times u_1(\phi_1)) & \boldsymbol{e}\cdot(x_2 \times u_2(\phi_2)) & \boldsymbol{e}\cdot(x_3 \times u_3(\phi_3)) \end{bmatrix} \begin{pmatrix} \lambda_1 \\ \lambda_2 \\ \lambda_3 \end{pmatrix} = \begin{pmatrix} 0 \\ 0 \\ 0 \end{pmatrix}. \tag{14}$$

Since this condition must be satisfied for nonzero magnitudes λ_i, the determinant of the 3×3 matrix in (14) must vanish, yielding a nonlinear equation in (ϕ_1, ϕ_2, ϕ_3), which is given by

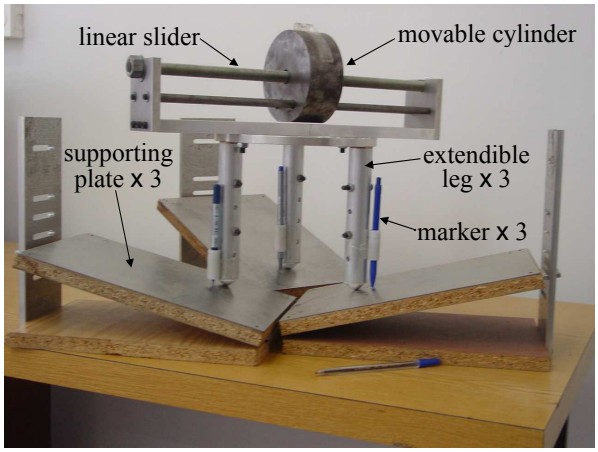

Figure 4: Experimental setup of a three-legged prototype.

(9) in Theorem 1. Equation (9) then implies that the torque balance (4b) is automatically satisfied, and the magnitudes λ_i are determined by solving the force balance (4a), giving a one-dimensional curve in (f_1, f_2, f_3)-space, which is then mapped to $\mathsf{bdy}(\widetilde{\mathcal{R}})$ via the map Ψ. □

5 Experimental Results

This section describes experiments that measure the equilibrium region of a three-legged prototype supported by a frictional terrain against gravity. The objective of these experiments is to validate the analytical characterization of the three types of boundary curves of the feasible equilibrium region, as well as their association with different modes of contact motions. The experimental system consists of a three-legged mechanism supported by three inclined plates (Figure 4). The mechanism is made of aluminium and consists of three extendible legs attached to a rigid ring. The central-ring diameter is 212 mm and the nominal length of each extendible leg is 180 mm. Each leg ends with a spherical footpad and maintains a point contact with its supporting plate. The mechanism's center of mass is determined by sliding a heavy steel cylinder mounted on top of the central ring. The cylinder moves along a linear slider of length 430 mm which can rotate in 15° increments. The mechanism's total weight is 7.9 kg, of which the movable steel cylinder weighs 4.2 kg. The plates supporting the mechanism have adjustable slopes. The (static) coefficient of friction between the footpads and plates was measured in a preliminary experiment, described as follows. The three-legged mechanism was placed on a single supporting plate, which was initially horizontal. The inclination angle of the plate was then slowly increased, until reaching a critical angle γ at which the mechanisms started to slide. The coefficient of friction μ is related to γ by $\mu = \tan(\gamma)$. Using this procedure, the average coefficient of friction was determined to be $\bar{\mu} = 0.26$ with a standard deviation of $\sigma = \pm 13\%$.

The process of measuring the boundary of $\widetilde{\mathcal{R}}$ is as follows. Each leg is equipped with a marker pressing lightly against its supporting plate (Figure 4). The mechanism is initially placed in static equilibrium on the supporting plates, with the sliding cylinder located above the mechanism's central ring. Next, we slowly slide the cylinder outward in 1 mm increments, pausing after each increment to check if any of the foot-markers has moved. This process

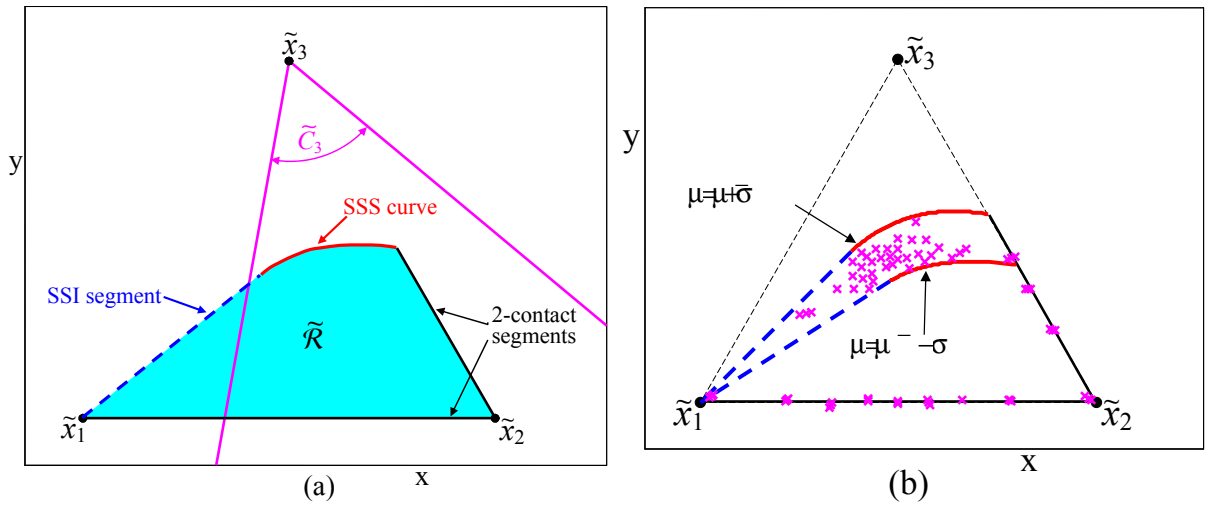

Figure 5: (a) Theoretical computation of $\widetilde{\mathcal{R}}$ (shaded region) for $\mu = \bar{\mu}$. (b) Experimental measurements of the critical center-of-mass positions ('×') compared with the theoretical boundaries of $\widetilde{\mathcal{R}}$ for $\mu = \bar{\mu} \pm \sigma$ (see text).

continues until the mechanism's center of mass reaches the boundary of the equilibrium region, where a critical event of contact breakage or slippage is observed. The critical center-of-mass position is recorded, and the process is repeated with the linear slider mounted at the next orientation. The slider's angles eventually cover a full circle with 15° resolution, giving a discrete mapping of the entire boundary of $\widetilde{\mathcal{R}}$.

The contacts selected for the experiment are positioned at equal heights and span a horizontal equilateral triangle having edge length of 165 mm. The supporting plates of x_1 and x_2 are set to be horizontal. The supporting plate of x_3 is set such that its contact normal makes a 30° angle with the upward direction $\boldsymbol{e}$, while its horizontal projection makes a 20° angle with the bisector of the equilateral triangle in a horizontal plane. Figure 5(a) shows a top view of the contacts and the horizontal projection of the friction cone C_3 (the horizontal projections of C_1 and C_2 span the entire plane). The theoretical region $\widetilde{\mathcal{R}}$ computed for the average value $\bar{\mu} = 0.26$ appears as a shaded region in Figure 5(a). Note that the boundary of $\widetilde{\mathcal{R}}$ consists of all three types of curves. Hence one expects three qualitatively distinct critical events in the experiment. Figure 5(b) shows the experimentally measured center-of-mass critical positions overlayed on the theoretical boundary of $\widetilde{\mathcal{R}}$. The experimental measurements are marked by '×.' The theoretical boundary of $\widetilde{\mathcal{R}}$ is computed for $\mu = \bar{\mu} + \sigma$ and $\mu = \bar{\mu} - \sigma$, and consists of two-contact segments (thick lines), three-contact SSI segments (dashed lines), and three-contact SSS curves (solid curves).

We now briefly discuss the results of the experiment. First note that the measurements along the two-contact segments have a very small variance. These measurements closely match the theoretical two-contact segments, except for measurements near x_1 and x_2 discussed below. The measurements associated with the SSI segments and SSS curves have a significantly larger variance. Yet all of these measurements fall within the region computed theoretically for the range $\bar{\mu} \pm \sigma$. Thus, *the theoretical computation of $\widetilde{\mathcal{R}}$ based on the model of point contact with Coulomb friction is validated.* The reason for the difference in the variances is as follows. Recall that two-contact segments are associated with onset of pure

rolling about two contacts and breakage of the third contact. The center-of-mass position on these segments depends solely on the position of the contacts, and can therefore be accurately measured irrespective of the value of μ. (An exception are measurements near x_1 and x_2 which are highly sensitive to the precise alignment of the linear slider with the contacts.) In contrast, measurements of points on the SSI segments and SSS curves are associated with onset of sliding at two or three contacts. The corresponding center-of-mass position is highly dependent on the coefficient of friction μ, whose value is determined experimentally and is subject to large deviations. These large deviation explain the high variance associated with measurements of points on the SSI segments and SSS curves. A possible reason for the large deviations in the measurements of μ is the fact that spherical footpads maintain only a point contact with the supports, which is highly sensitive to surface irregularities. A practical solution to this problem would be to "flatten" the footpads in order to distribute the contacts over small areas. Note, however, that in this case one should use a soft-finger contact model [30].

6 Conclusion

This paper characterized the feasible equilibrium region on uneven terrains for *tame* 3-contact arrangements, where the friction cones lie above the plane spanned by the contacts. The paper first established that the feasible equilibrium region forms a right cylinder whose convex cross-section $\widetilde{\mathcal{R}}$ lies within the contacts' support polygon. The paper then showed that the boundary of $\widetilde{\mathcal{R}}$ consists of three types of curves: two-contact linear segments, three-contact SSI linear segments, and three-contact SSS curves. The first two types possess closed form formulas which depend on the geometric data and the coefficient of friction μ. The three-contact SSS curves are highly nonlinear and possess only an implicit formulation in (ϕ_1, ϕ_2, ϕ_3)-space. However, each SSS curve on the boundary of $\widetilde{\mathcal{R}}$ lies between linear segments, making the SSS curves fully traceable. The paper subsequently associated the three types of boundary curves with the potential onset of non-static contact modes: the two-contact segments are associated with two rolling contacts and one breaking-off contact; the SSI segments are associated with two sliding contacts and one rolling contact; the SSS curves are associated with three sliding contacts. Experimental measurements using a three-legged prototype corroborated the analytic characterization of the three types of boundary curves of $\widetilde{\mathcal{R}}$, as well as their association with the different non-static contact modes.

We now briefly discuss several future extensions of the results. A first extension is computation of the feasible equilibrium region associated with $k > 3$ contacts. The support polygon, $\widetilde{\mathcal{P}}$, is still the convex hull of the horizontally projected contacts. However, now only a subset of the contacts contributes vertices to $\widetilde{\mathcal{P}}$. Let $x_1, \ldots x_p$ $(p \leq k)$ be the contacts associated with the vertices of $\widetilde{\mathcal{P}}$, where the contacts are enumerated consecutively along the boundary of $\widetilde{\mathcal{P}}$. Then a k-contact arrangement will be defined as *tame* if for each pair of contacts x_i, x_{i+1} (where i is counted modulo p), the triplet (x_i, x_{i+1}, x_j) forms a tame 3-contact arrangement where x_j varies over all remaining contacts. The tame k-contact arrangements still satisfy the key relation $\widetilde{\mathcal{R}} \subseteq \widetilde{\mathcal{P}}$. Our current research indicates that the boundary of $\widetilde{\mathcal{R}}$ consists of the same three types of curves associated with two or three active contacts, together with new types of curves associated with higher number of contacts. Efficient enumeration of the new curves as well as experimental verification of the resulting

equilibrium region are currently under investigation.

A second possible extension is accounting for *non-tame* contact arrangements, which are typical to scenarios of vertical climbing. In that case, the feasible equilibrium region is not bounded within the support polygon, and may even lie entirely *outside* the support polygon (see example in [6]). Though the existing types of boundary curves of $\widetilde{\mathcal{R}}$ do not change in such scenarios, a problem may arise if $\widetilde{\mathcal{R}}$ becomes *unbounded* in some directions. Note that the computational algorithms in [5] and [6] also fail to work in these cases, since they require an initial guess of a polygon $\widetilde{\mathcal{R}}$ from the outside. A systematic method for identifying contact arrangements resulting in unbounded $\widetilde{\mathcal{R}}$, as well as its computation, are still an open problem.

A third future direction is merging our results with the computational algorithm proposed in [6]. Note that the algorithm in [6] iteratively computes outer and inner polygonal approximations of $\widetilde{\mathcal{R}}$, whereas two of three types of the *exact* boundary of $\widetilde{\mathcal{R}}$ are linear segments that are given here in closed form, and have a clear geometric interpretation. Computing these boundary segments in a preliminary step and using them as initial guesses for the algorithm of [6] may reduce its computational cost. The improved algorithm can be utilized to enhance the performance of motion planning based on fast sampling of a high-dimensional configuration space [4, 19], or even for ongoing efforts on explicit motion planning on rough terrain [50].

Finally, a longer term issue is the construction of quasistatic locomotion planners based on feasible equilibrium regions. While it is tempting to demonstrate the utility of such planners, equilibrium feasibility must first be augmented with the following additional considerations. The first consideration concerns the ambiguous rigid-body dynamics incurred by the presence of friction at the contacts [26, 31, 49]. One must ensure that a feasible equilibrium is dynamically non-ambiguous, or a *strong equilibrium* [27, 44]. A second issue concerns the *stability* of a candidate equilibrium posture, which consists of two types of stability. First, a candidate equilibrium posture must be able to resist disturbance wrenches generated by moving parts of the mechanism. This notion has been treated as *posture robustness* in planar environments [42], and its characterization in three-dimensions is currently under investigation. Second, a candidate equilibrium posture must be dynamically stable with respect to position-and-velocity perturbations. This classical type of stability must account for the hybrid dynamics induced by non-smooth transitions associated with contact slippage, contact breakage, and impacts at recovering contacts. Some initial progress is reported for specific scenarios [14, 18, 45]. However, a general stability theory for multi-contact systems undergoing impacts is a primary open problem in the area of non-smooth mechanical systems [41, 43].

Acknowledgement

We wish to thank one of the anonymous reviewers for careful reading and detailed comments that greatly improved the quality and clarity of this paper.

A Appendix - Proofs and Technical Details

Proof of Proposition : 3.1: First consider the case of a tame contact arrangement. We have to show that any center-of-mass position satisfying the equilibrium condition (1) lies in $\mathcal{P}$. Let l_{12} denote the spatial line passing through x_1 and x_2. Since f_1 and f_2 generate zero torque about l_{12}, the torque-balance part of (1) implies that the net torque generated by f_g and f_3 about l_{12} must vanish. Since the contact arrangement is tame, f_3 satisfies $f_3 \cdot \boldsymbol{\nu} \geq 0$. Hence torque balance about l_{12} can be shown to imply that $\boldsymbol{x}$ must lie within the semi-infinite halfspace bounded by the vertical plane passing through x_1 and x_2 which contains x_3. Repeating this argument for the other two contact permutations, we obtain that $\boldsymbol{x}$ must lie within the right prism spanned by the contacts, which is precisely $\mathcal{P}$. Thus $\mathcal{R} \subseteq \mathcal{P}$.

Next consider the case of a quasi-flat contact arrangement. Since $\boldsymbol{e} \in C_i$, a single vertical contact force, $f_i = -f_g$, can balance the gravitational force. Hence the entire vertical line through x_i lies in $\mathcal{R}$ $(i = 1, 2, 3)$. According to Proposition 2.1, $\mathcal{R}$ is a convex set. Hence $\mathcal{R}$ contains the right prism spanned by the contacts, which is precisely $\mathcal{P}$. □

Proof of Lemma 4.2: The boundary of C_1 is the union $\mathsf{bdy}(C_1) = \{0\} \cup S_1$. Hence $\mathsf{bdy}(C_1) \times C_2 \times C_3 = \{0\} \times C_2 \times C_3 \cup S_1 \times C_2 \times C_3$. We now proceed with each of the two sets. Writing C_2 and C_3 as the union: $C_j = \mathsf{int}(C_j) \cup S_j \cup \{0\}$ $(j = 2, 3)$, the subdivision of the first set is: $\{0\} \times C_2 \times C_3 = \{0\} \times \mathsf{int}(C_2) \times S_3 \cup \{0\} \times S_2 \times \mathsf{int}(C_3) \cup \{0\} \times \mathsf{int}(C_2) \times \mathsf{int}(C_3)$, where we omitted cells of dimension less than five. This gives two of the 5D cells in item 1, and the 6D cell of item 2. The subdivision of the second set is: $S_1 \times C_2 \times C_3 = S_1 \times \{0\} \times C_3 \cup S_1 \times S_2 \times C_3 \cup S_1 \times \mathsf{int}(C_2) \times C_3$, where again we omitted lower dimensional cells. The first set contains the cell $S_1 \times \{0\} \times \mathsf{int}(C_3)$, which is one of the 5D cells in item 1. The subdivision of the second set is: $S_1 \times S_2 \times C_3 = S_1 \times S_2 \times S_3 \cup S_1 \times S_2 \times \mathsf{int}(C_3)$. This gives the 6D cell of item 3 and one of the 7D cells in item 4. The subdivision of the third set is: $S_1 \times \mathsf{int}(C_2) \times C_3 = S_1 \times \mathsf{int}(C_2) \times \{0\} \cup S_1 \times \mathsf{int}(C_2) \times S_3 \cup S_1 \times \mathsf{int}(C_2) \times \mathsf{int}(C_3)$. It gives one of the 5D cells in item 1, one of the 7D cells in item 4, and the 8D cell of item 5. □

Useful facts from line geometry: The ensuing analysis is based on results from line geometry for which we need some terminology [10, 33, 48, 52]. Let l be a spatial line passing through a point p along a direction v. The *Plücker coordinates* of l are defined as $(v, p \times v) \in \mathbb{R}^6$. For collections of spatial lines, the linear subspaces spanned by their Plücker coordinates in $\mathbb{R}^6$ have well known characterizations. In particular, a two-dimensional linear subspace spanned by $(v_1, p \times v_1)$ and $(v_2, p \times v_2)$ is a *flat pencil*. It is the collection of all spatial lines passing through p and embedded in a plane spanned by (v_1, v_2). A three-dimensional linear subspace spanned by $(v_1, p \times v_1)$,$(v_2, p \times v_2)$,$(v_3, p \times v_3)$ is a *solid pencil*. It is the collection of all lines passing through p along all spatial directions. The next lemma provides useful facts from line geometry, which are utilized in the proofs of Proposition 4.3 and Proposition 4.4. The lemma is based on the following geometric properties of spatial lines [10, 33, 48, 52]. First, three spatial lines possess linearly dependent Plücker coordinates iff they lie on a common flat pencil. Second, two spatial lines having Plücker coordinates $(v_1, x_1 \times v_1)$ and $(v_2, x_2 \times v_2)$ are *reciprocal* if $(v_1, p_1 \times v_1) \cdot (p_2 \times v_2, v_2) = 0$ (note the transposed coordinates of the second line). It is a basic geometric fact that two lines are reciprocal iff they intersect in physical space.

Lemma A.1. *Let x_1, x_2, x_3 be three points in $\mathbb{R}^3$ which do not lie along a common spatial line. Then the following relations hold for pencils at these points.*

1. *Three flat pencils at x_1, x_2, x_3 are linearly dependent iff they intersect at a common point on the plane Δ spanned by the three points.*
2. *Two flat pencils at x_1, x_2 and one solid pencil at x_3 are linearly dependent iff the two flat pencils intersect at x_3.*
3. *One flat pencil at x_1 and two solid pencils at x_2, x_3 are linearly dependent iff the flat pencil coincides with the plane Δ spanned by the three points.*

Proof: First consider the case of three flat pencils at x_1, x_2, x_3. Let $(u_i, x_i \times u_i)$ and $(v_i, x_i \times v_i)$ be the Plücker coordinates of two lines spanning the i^{th} flat pencil $(i = 1, 2, 3)$. Linear dependence of the six lines requires that the columns of the following 6×6 matrix be linearly dependent,

$$A_1 = \begin{pmatrix} u_1 & v_1 & u_2 & v_2 & u_3 & v_3 \\ x_1 \times u_1 & x_1 \times v_1 & x_2 \times u_2 & x_2 \times v_2 & x_3 \times u_3 & x_3 \times v_3 \end{pmatrix}.$$

A linear combination of each pair of columns associated with x_i gives a line in the i^{th} flat pencil $(i = 1, 2, 3)$. Hence linear dependence of the columns is equivalent to linear dependence in Plücker coordinates of some three lines associated with the three flat pencils. Let l_1, l_2, l_3 denote these three lines. Then l_1, l_2, l_3 must belong to a common flat pencil in $\mathbb{R}^3$. Since l_i passes through x_i for $i = 1, 2, 3$, the latter flat pencil coincides with the plane Δ spanned by the points $\{x_1, x_2, x_3\}$. It follows that each l_i is the intersection of the i^{th} flat pencil with Δ $(i = 1, 2, 3)$. Since l_1, l_2, l_3 belong to a common flat pencil they pass through a common point in Δ. Hence the original flat pencils intersect at a common point in Δ.

Next, consider the case of two flat pencils at x_1, x_2 and a solid pencil at x_3. Let $(u_i, x_i \times u_i)$ and $(v_i, x_i \times v_i)$ be two lines spanning the i^{th} flat pencil $(i = 1, 2)$. Let $(u_3, x_3 \times u_3)$, $(v_3, x_3 \times v_3)$, $(w_3, x_3 \times w_3)$ be three lines spanning the solid pencil at x_3. We may set $x_3 = 0$ without loss of generality, so that the Plücker coordinates of the lines spanning the solid pencil become $(u_3, 0)$, $(v_3, 0)$, $(w_3, 0)$. Linear dependence of the seven lines requires that the *rows* of the following 6×7 matrix be linearly dependent,

$$A_2 = \begin{pmatrix} u_1 & v_1 & u_2 & v_2 & u_3 & v_3 & w_3 \\ x_1 \times u_1 & x_1 \times v_1 & x_2 \times u_2 & x_2 \times v_2 & 0 & 0 & 0 \end{pmatrix},$$

The rows of A_2 are linearly dependent iff there exist a nonzero row vector $(v, w) \in \mathbb{R}^6$ such that $(v, w)A_2 = 0$, where $0 \in \mathbb{R}^7$. In particular, $(v, w)[u_3\, v_3\, w_3] = 0$ implies that $v = 0$. The left-kernel of A_2 is therefore spanned by $(0, w)$. In Plücker coordinates, $(w, 0)$ represents a spatial line passing through $x_3 = 0$ along the direction w. It follows that linear dependence of A_2's rows is equivalent to the existence of a spatial line l passing through x_3 which is reciprocal to all lines of the two flat pencils. Using the geometric fact concerning reciprocality, l must coincide with the intersection line of the two flat pencils. Since l passes through x_3, the two flat pencils pass through x_3.

Last, consider the case of a flat pencil at x_1 and two solid pencils at x_2 and x_3. The flat pencil is spanned by two lines and each of the solid pencils is spanned by three lines. Denoting the eight lines as above, linear dependence of these lines requires that the rows of

the following 6×8 matrix be linearly dependent,

$$A_3 = \begin{pmatrix} u_1 & v_1 & u_2 & v_2 & w_2 & u_3 & v_3 & w_3 \\ x_1 \times u_1 & x_1 \times v_1 & x_2 \times u_2 & x_2 \times v_2 & x_2 \times w_2 & 0 & 0 & 0 \end{pmatrix},$$

where we set again $x_3 = 0$. Here, too, the left-kernel of A_3 is spanned by $(0, w) \in I\!R^6$. Reciprocality of $(0, w)$ with the first five columns of A_3 dictates existence of a line l passing through x_3 along the direction w, such that l intersects all lines of the flat pencil at x_1 and all lines of the solid pencil at x_2. The only way l can intersect all lines of the solid pencil is by passing through its base point x_2. It follows that the line joining x_2 and x_3 lies in the flat pencil at x_1, implying that the flat pencil at x_1 coincides with the plane Δ.

Finally, the geometric conditions specified in items 1,2,3 give rank deficient matrices A_1, A_2, A_3, which imply the pencils' linear dependency specified in the lemma. □

Proof of Proposition 4.3: We have to inspect the image under $\mathcal{L}$ of each cell in items 1-5. The 5D cells listed in item 1 are generically mapped by $\mathcal{L}$ into five-dimensional sets in W. Since the boundary of W is also five-dimensional, all 5D cells are potential sources for five-dimensional boundary pieces of W. For each cell of dimension six or higher, a necessary condition that its image under $\mathcal{L}$ would contribute to the boundary of W is that *the Jacobian of the restriction of $\mathcal{L}$ to the cell would lose its rank.* Hence we must check the Jacobian of $\mathcal{L}$ on each cell listed in items 2-5.

First consider the 6D cell $\{0\} \times \mathsf{int}(C_2) \times \mathsf{int}(C_3)$ of item 2. Let $\mathcal{L}_1$ denote the restriction of $\mathcal{L}$ to this cell. Using (f_2, f_3) to parametrize this cell, $\mathcal{L}_1$ is a mapping from $I\!R^6$ into $I\!R^6$. The Jacobian of $\mathcal{L}_1$ is the 6×6 matrix:

$$J_1 = \begin{pmatrix} I & I \\ [x_2\times] & [x_3\times] \end{pmatrix} \sim \begin{pmatrix} O & I \\ [(x_2 - x_3)\times] & O \end{pmatrix},$$

where I is a 3×3 identity matrix, O is a 3×3 matrix of zeroes, and $[x_i\times]$ is a 3×3 skew-symmetric matrix satisfying $[x_i\times]v = x_i \times v$ for all $v \in I\!R^3$. The Jacobian J_1 has a one-dimensional kernel spanned by the column vector $(x_2 - x_3, 0) \in I\!R^6$. Hence the entire image of $\{0\} \times \mathsf{int}(C_2) \times \mathsf{int}(C_3)$ under $\mathcal{L}$ is a five-dimensional set in W. Since the boundary of W is also five-dimensional, the entire cell is a potential source for a five-dimensional boundary piece of W.

Next consider the 6D cell $S_1 \times S_2 \times S_3$ of item 3. Let $\mathcal{L}_2$ denote the restriction of $\mathcal{L}$ to this cell. Using (λ_i, ϕ_i) to parametrize the friction-cone boundary S_i $(i = 1, 2, 3)$, $\mathcal{L}_2$ is a mapping from $I\!R^6$ into $I\!R^6$. The Jacobian of $\mathcal{L}_2$ is the 6×6 matrix:

$$J_2 = \begin{pmatrix} u_1(\phi_1) & \lambda_1 u_1'(\phi_1) & u_2(\phi_2) & \lambda_2 u_2'(\phi_2) & u_3(\phi_3) & \lambda_3 u_3'(\phi_3) \\ x_1 \times u_1(\phi_1) & \lambda_1 x_1 \times u_1'(\phi_1) & x_2 \times u_2(\phi_2) & \lambda_2 x_2 \times u_2'(\phi_2) & x_3 \times u_3(\phi_3) & \lambda_3 x_3 \times u_3'(\phi_3) \end{pmatrix}. \tag{15}$$

Each column of J_2 represents in Plücker coordinates a spatial line passing through x_i with direction $u_i(\phi_i)$ or $u_i'(\phi_i)$ $(i = 1, 2, 3)$. Since $(u_i(\phi_i), u_i'(\phi_i))$ spans the tangent plane to S_i, each pair of columns spans a flat pencil tangent to S_i and passing through x_i. We now invoke a result from line geometry which appears in [52] and is reviewed in Lemma A.1. If x_1, x_2, x_3 do not lie on a common spatial line, three flat pencils at x_1, x_2, x_3 are linearly dependent iff they intersect at a common point on the base plane Δ. This condition identifies the subset of $S_1 \times S_2 \times S_3$ which is possibly mapped to a five-dimensional boundary piece of

W. The subset consists of contact forces $f_i(\lambda_i, \phi_i)$ such that the intersection point of the three tangent planes $\Delta_i(\phi_i)$ lies on the base plane Δ. An equivalent condition is that the lines $\{l_1, l_2, l_3\}$ intersect at a common point, where l_i denotes the line of intersection of the tangent plane $\Delta_i(\phi_i)$ with the base plane Δ for $i = 1, 2, 3$. This condition implies the linear dependency of the Plücker coordinates of l_i, which are given by $(\boldsymbol{\nu} \times \boldsymbol{\eta}_i(\phi_i), x_i \times \boldsymbol{\nu} \times \boldsymbol{\eta}_i(\phi_i))$. Since the lines l_i all lie on Δ, the linear dependency condition can be reduced to vanishing of the determinant given in (10).

Consider now the 7D cell $S_1 \times S_2 \times \mathsf{int}(C_3)$ of item 4 (the other 7D cell can be analyzed in a similar manner). Let $\mathcal{L}_3$ denote the restriction of $\mathcal{L}$ to this cell. Using (λ_i, ϕ_i) to parametrize S_i $(i = 1, 2)$ and f_3 to parametrize $\mathsf{int}(C_3)$, $\mathcal{L}_3$ is a mapping from $\mathbb{R}^7$ into $\mathbb{R}^6$. The Jacobian of $\mathcal{L}_3$ is the 6×7 matrix:

$$J_3 = \begin{pmatrix} u_1(\phi_1) & \lambda_1 u_1'(\phi_1) & u_2(\phi_2) & \lambda_2 u_2'(\phi_2) & I \\ x_1 \times u_1(\phi_1) & \lambda_1 x_1 \times u_1'(\phi_1) & x_2 \times u_2(\phi_2) & \lambda_2 x_2 \times u_2'(\phi_2) & [x_3 \times] \end{pmatrix}. \tag{16}$$

The four columns of J_3 associated with x_1 and x_2 span two flat pencils tangent to S_1 and S_2. The three columns associated with x_3 span a solid pencil at x_3. We now invoke a second fact from Lemma A.1. If x_1, x_2, x_3 do not lie along a common spatial line, two flat pencils at x_1, x_2 and one solid pencil at x_3 are linearly dependent iff the two flat pencils intersect at x_3. This condition identifies the subset of $S_1 \times S_2 \times \mathsf{int}(C_3)$ which is possibly mapped to a five-dimensional boundary piece of W.

Finally consider the 8D cell $S_1 \times \mathsf{int}(C_2) \times \mathsf{int}(C_3)$. Let $\mathcal{L}_4$ denote the restriction of $\mathcal{L}$ to this cell. Using (λ_1, ϕ_1) to parametrize S_1 and (f_2, f_3) to parametrize $\mathsf{int}(C_2) \times \mathsf{int}(C_3)$, $\mathcal{L}_4$ is a mapping from $\mathbb{R}^8$ into $\mathbb{R}^6$. The Jacobian of $\mathcal{L}_4$ is the 6×8 matrix:

$$J_4 = \begin{pmatrix} u_1(\phi_1) & \lambda_1 u_1'(\phi_1) & I & I \\ x_1 \times u_1(\phi_1) & \lambda_1 x_1 \times u_1'(\phi_1) & [x_2 \times] & [x_3 \times] \end{pmatrix}.$$

The two columns of J_4 associated with x_1 span a flat pencil tangent to S_1. The six columns associated with x_2 and x_3 span two solid pencils at x_2 and x_3. We now invoke a third fact from Lemma A.1. If x_1, x_2, x_3 do not lie on a common spatial line, one flat pencil at x_1 and two solid pencils at x_2 and x_3 are linearly dependent iff the flat pencil at x_1 coincides with the base plane Δ. It follows that $\mathcal{L}_4$ loses rank on the 8D cell only when C_1 is tangent to the base plane Δ. For a tame contact arrangement, C_1 lies strictly above Δ. Hence $\mathcal{L}_4$ has full rank on the entire cell, and the cell is mapped into the interior of W. □

Proof of Proposition 4.4: First consider the closed 6D cell $\{0\} \times C_2 \times C_3$ (the other cells of item 1 can be similarly analyzed). Let l_{23} denote the spatial line passing through x_2 and x_3. Since the forces $(f_2, f_3) \in C_2 \times C_3$ generate zero torque about l_{23}, the image of $\{0\} \times C_2 \times C_3$ under $\mathcal{L}$ is embedded in a five-dimensional linear subspace in wrench space. This subspace, denoted U, is orthogonal to a pure-torque wrench about l_{23}. The image of $\{0\} \times C_2 \times C_3$ under $\mathcal{L}$ lies on the boundary of W if all forces $(f_1, f_2, f_3) \in C_1 \times C_2 \times C_3$ generate net wrenches in the *same* halfspace bounded by U in wrench space. Since the contact arrangement is tame, the entire friction cone C_1 lies on one side of the base plane Δ. Since l_{23} lies in Δ, all forces of C_1 generate the same torque sign about l_{23}. Hence all forces in $C_1 \times C_2 \times C_3$ generate the same torque sign about l_{23}. Since a pure-torque wrench about l_{23} is orthogonal to U in wrench space, we established that all forces in $C_1 \times C_2 \times C_3$ generate net wrenches in the same halfspace bounded by U. The closed 6D cell $\{0\} \times C_2 \times C_3$ is thus mapped by $\mathcal{L}$ to the boundary of W.

Next consider the 7D cell $S_1 \times S_2 \times \mathsf{int}(C_3)$. According to Proposition 4.3, only the subset of forces $(f_1, f_2) \in S_1 \times S_2$ whose tangent planes intersect at x_3 while $f_3 \in \mathsf{int}(C_3)$ is mapped to a five-dimensional manifold in W. Let $\boldsymbol{w}_0$ be a particular wrench on this manifold, generated by $(f_1^0, f_2^0, f_3^0) \in S_1 \times S_2 \times \mathsf{int}(C_3)$, and let V denote the manifold's five-dimensional tangent space at $\boldsymbol{w}_0$. The wrench $\boldsymbol{w}_0$ lies on the boundary of W if all forces $(f_1, f_2, f_3) \in C_1 \times C_2 \times C_3$ generate net wrenches in the *same* halfspace bounded by V. The wrench orthogonal to V is the left kernel of the Jacobian of $\mathcal{L}$ evaluated on the 7D cell. This Jacobian is the 6×7 matrix J_3 specified in (16). Selecting the origin at x_3 and recalling that $f_i(\lambda_i, \phi_i) = \lambda_i u(\phi_i)$ $(i = 1, 2)$, the Jacobian is given by

$$J_3 = \begin{pmatrix} u_1(\phi_1) & \lambda_1 u_1'(\phi_1) & u_2(\phi_2) & \lambda_2 u_2'(\phi_2) & I \\ x_1 \times u_1(\phi_1) & \lambda_1 x_1 \times u_1'(\phi_1) & x_2 \times u_2(\phi_2) & \lambda_2 x_2 \times u_2'(\phi_2) & O \end{pmatrix},$$

where (ϕ_i, λ_i) for $i = 1, 2$ correspond to (f_1^0, f_2^0), I is a 3×3 identity matrix, and O is a 3×3 zero matrix. The last three columns of J_3 imply that its left kernel is spanned by the row vector $(0, \tau_0)$, where τ_0 is yet to be determined. Let l denote the line of intersection of the tangent planes $\Delta_1(\phi_1)$ and $\Delta_2(\phi_2)$, whose direction is given by $\hat{l} = \boldsymbol{\eta}_1(\phi_1) \times \boldsymbol{\eta}_2(\phi_2)$. The vectors x_i and $u_i(\phi_i), u_i'(\phi_i)$ lie in $\Delta_i(\phi_i)$. Hence $x_i \times u_i(\phi_i)$ and $x_i \times u_i'(\phi_i)$ are orthogonal to $\hat{l}$ $(i = 1, 2)$. The left kernel of J_3 is therefore spanned by the row vector $(0, \tau_0) = (0, \hat{l})$. The halfspace bounded by V in wrench space is: $\{(f, \tau) : (0, \hat{l}) \cdot (f, \tau) = \hat{l} \cdot \tau \geq 0\}$. It follows that all forces of $C_1 \times C_2 \times C_3$ must generate the same torque sign about l. The forces $f_3 \in C_3$ generate zero torque about l. The line l lies in the tangent plane of $f_i^0 \in S_i$ $(i = 1, 2)$. It can be verified that consequently all forces $f_i \in C_i$ generate the same torque sign about l $(i = 1, 2)$. Hence it suffices to check the torque sign about l of representative forces from the interiors of C_1 and C_2. Using the contact normals $\boldsymbol{n}_1$ and $\boldsymbol{n}_2$ for this purpose, we obtain condition (8).

Consider now the 6D cell $S_1 \times S_2 \times S_3$. According to Proposition 4.3, only the subset of forces (f_1, f_2, f_3) whose tangent planes intersect at a common point $z \in \Delta$ is mapped by $\mathcal{L}$ to a five-dimensional manifold in W. Let $\boldsymbol{w}_0$ be a particular wrench on this manifold, generated by $(f_1^0, f_2^0, f_3^0) \in S_1 \times S_2 \times S_3$, and let V denote the manifold's tangent space at $\boldsymbol{w}_0$. If $\boldsymbol{w}_0$ lies on the boundary of W, all local force variations $(f_1^0, f_2^0, f_3^0) + (\Delta f_1, \Delta f_2, \Delta f_3) \in C_1 \times C_2 \times C_3$ must generate net wrenches in the *same* halfspace bounded by V. The wrench orthogonal to V is the left kernel of the Jacobian of $\mathcal{L}$ evaluated on $S_1 \times S_2 \times S_3$. This Jacobian is the 6×6 matrix J_2 specified in (15) and given by

$$J_2 = \begin{pmatrix} u_1(\phi_1) & \lambda_1 u_1'(\phi_1) & u_2(\phi_2) & \lambda_2 u_2'(\phi_2) & u_3(\phi_3) & \lambda_3 u_3'(\phi_3) \\ x_1 \times u_1(\phi_1) & \lambda_1 x_1 \times u_1'(\phi_1) & x_2 \times u_2(\phi_2) & \lambda_2 x_2 \times u_2'(\phi_2) & x_3 \times u_3(\phi_3) & \lambda_3 x_3 \times u_3'(\phi_3) \end{pmatrix},$$

where (ϕ_i, λ_i) for $i = 1, 2, 3$ correspond to (f_1^0, f_2^0, f_3^0). Each pair $(u_i(\phi_i), u_i'(\phi_i))$ spans the tangent plane of $f_i^0 \in S_i$. Hence a suitable linear combination of $u_i(\phi_i)$ and $u_i'(\phi_i)$ gives a vector lying in the base plane Δ, denoted v_i for $i = 1, 2, 3$. Since the three tangent planes intersect at $z \in \Delta$, each v_i is collinear with $x_i - z$. Selecting the origin at z, the Jacobian J_2 can be equivalently written as

$$J_2 \sim \begin{pmatrix} u_1(\phi_1) & v_1 & u_2(\phi_2) & v_2 & u_3(\phi_3) & v_3 \\ x_1 \times u_1(\phi_1) & 0 & x_2 \times u_2(\phi_2) & 0 & x_3 \times u_3(\phi_3) & 0 \end{pmatrix}.$$

Recall that $\boldsymbol{\nu}$ is the unit normal to Δ. Since v_1, v_2, v_3 lie in Δ, the columns $(v_1, 0), (v_2, 0), (v_3, 0)$ imply that the left kernel of J_2 is spanned by the row vector $(\boldsymbol{\nu}, \tau_0)$, where τ_0 is yet to be

determined. Rather than explicitly compute τ_0, we express it in terms of two parameters: $x_b = \tau_0 \times \boldsymbol{\nu} \in \Delta$ and $p = \tau_0 \cdot \boldsymbol{\nu} \in \mathbb{R}$ (these parameters are the action point and pitch of the force screw associated with the left kernel of J_2). The expression for τ_0 in terms of x_b and p is $\tau_0 = x_b \times \boldsymbol{\nu} + p\boldsymbol{\nu}$.

Recall that $\boldsymbol{\eta}_i$ is the unit normal to the tangent plane of $f_i^0 \in S_i$, pointing into the interior of C_i for $i = 1, 2, 3$. Let $\bar{\boldsymbol{\nu}}_i$ denote the projection of $\boldsymbol{\eta}_i$ on the base plane Δ, $\bar{\boldsymbol{\nu}}_i = [I - \boldsymbol{\nu}\boldsymbol{\nu}^T]\boldsymbol{\eta}_i$. Since the contact arrangement is tame, each C_i lies strictly above Δ. Hence $\bar{\boldsymbol{\nu}}_i$ is non-vanishing and points into the interior of C_i for $i = 1, 2, 3$. Any local variation $f_i^0 + \Delta f_i \in C_i$ can be written as $\Delta f_i = \Delta f_{i1} + \Delta f_{i2}$, such that Δf_{i1} is tangent to S_i at f_i^0 while $\Delta f_{i2} = \kappa_i \bar{\boldsymbol{\nu}}_i$ for some $\kappa_i \geq 0$. We now derive a condition guaranteeing that the wrenches generated by $f_i^0 + \Delta f_i \in C_i$ for $i = 1, 2, 3$ lie in the same halfspace bounded by V. The wrench generated by $f_i^0 + \Delta f_{i1}$ is spanned by the two columns of J_2 associated with the i^{th} contact. This wrench is therefore orthogonal to the left kernel of J_2. The wrench generated by $\Delta f_{i2} = \kappa_i \bar{\boldsymbol{\nu}}_i$ satisfies $(\boldsymbol{\nu}, \tau_0) \cdot (\Delta f_{i2}, x_i \times \Delta f_{i2}) = \kappa_i \, \tau_0 \cdot (x_i \times \bar{\boldsymbol{\nu}}_i)$, where we used the fact that $\boldsymbol{\nu} \cdot \bar{\boldsymbol{\nu}}_i = 0$. Recall now that the origin is set at $z \in \Delta$, so that x_i lies in Δ for $i = 1, 2, 3$. Substituting $\tau_0 = x_b \times \boldsymbol{\nu} + p\boldsymbol{\nu}$, we obtain $\kappa_i \, \tau_0 \cdot (x_i \times \bar{\boldsymbol{\nu}}_i) = p \, \kappa_i \, \boldsymbol{\nu} \cdot (x_i \times \bar{\boldsymbol{\nu}}_i)$, where we used the fact that $x_b \times \boldsymbol{\nu}$ lies in Δ while $x_i \times \bar{\boldsymbol{\nu}}_i$ is orthogonal to Δ. Finally $\boldsymbol{\nu} \times \bar{\boldsymbol{\nu}}_i = \boldsymbol{\nu} \times \boldsymbol{\eta}_i$, so we can use $\boldsymbol{\eta}_i$ rather than its projection $\bar{\boldsymbol{\nu}}_i$. Thus, all local force variations generate net wrenches in the same halfspace bounded by V if the terms $p \, \kappa_i \, \boldsymbol{\nu} \cdot (x_i \times \boldsymbol{\eta}_i)$ possess the same sign for $i = 1, 2, 3$. The sign agreement of the three terms is unaffected by the common factor p and by the non-negative scalars s_1, s_2, s_3. Hence we obtain condition (11). This condition ensures that all local force variations about (f_1^0, f_2^0, f_3^0) in $C_1 \times C_2 \times C_3$ generate net wrenches in the same halfspace based at $\boldsymbol{w}_0$ and bounded by V. We now show that $\boldsymbol{w}_0$ consequently lies on the boundary of W. The linear map $\mathcal{L}$ maps rays in (f_1, f_2, f_3)-space to rays in wrench space. Consider now the collection of rays $(f_1^0, f_2^0, f_3^0) + s(\Delta f_1, \Delta f_2, \Delta f_3)$ such that $(f_1^0, f_2^0, f_3^0) + (\Delta f_1, \Delta f_2, \Delta f_3) \in C_1 \times C_2 \times C_3$ and $s \geq 0$. These rays span the (f_1, f_2, f_3)-halfspace bounded by the tangent space to $C_1 \times C_2 \times C_3$ at (f_1^0, f_2^0, f_3^0). Since $C_1 \times C_2 \times C_3$ is convex, it is wholly contained in the latter halfspace. Condition (11) implies that the above collection of rays is mapped by $\mathcal{L}$ to a collection of rays which spans the halfspace based at $\boldsymbol{w}_0$ and bounded by V. Since W is the image of $C_1 \times C_2 \times C_3$ under $\mathcal{L}$, it lies wholly in this halfspace, implying that $\boldsymbol{w}_0$ lies on the boundary of W. □

Proof Sketch for Corollary 4.1: Since (ϕ_1, ϕ_2, ϕ_3)-space is compact, the implicit solution of (9) and (10) consists of several disjoint loops. These loops are mapped by (5) to possibly overlapping SSS loops in $\widetilde{\mathcal{R}}$. According to Proposition 4.4, any portion of an SSS loop on the boundary of $\widetilde{\mathcal{R}}$ is the image under (5) of points (ϕ_1, ϕ_2, ϕ_3) satisfying

$$\mathsf{sgn}\big(\boldsymbol{\nu} \cdot ((x_1 - z) \times \boldsymbol{\eta}_1(\phi_1))\big) = \mathsf{sgn}\big(\boldsymbol{\nu} \cdot ((x_2 - z) \times \boldsymbol{\eta}_2(\phi_2))\big) = \mathsf{sgn}\big(\boldsymbol{\nu} \cdot ((x_3 - z) \times \boldsymbol{\eta}_3(\phi_3))\big), \quad (17)$$

where $z(\phi_1, \phi_2, \phi_3) \in \Delta$ is the common intersection point of the tangent planes of $f_i \in S_i$ for $i = 1, 2, 3$. If an SSS loop lies partially on the boundary of $\widetilde{\mathcal{R}}$, its portion on the boundary has two endpoints p_1 and p_2. Beyond these endpoints the SSS loop locally lies in the interior of $\widetilde{\mathcal{R}}$, implying that one of the terms in (17) switches its sign beyond p_1 and p_2. A continuity argument implies that this particular term must vanish at p_1 and p_2.

We now show that all terms in (17) are non-vanishing on the 6D cell $S_1 \times S_2 \times S_3$ as long as $z(\phi_1, \phi_2, \phi_3) \neq x_i$ $(i = 1, 2, 3)$. Recall that $\Delta_i(\phi_i)$ is the tangent plane of $f_i \in S_i$. For a tame contact arrangement $\Delta_i(\phi_i)$ is transversal to the base plane Δ. By construction $\boldsymbol{\nu} \neq 0$ is orthogonal to Δ, $\boldsymbol{\eta}_i \neq 0$ is orthogonal to $\Delta_i(\phi_i)$, while $x_i - z \neq 0$ lies in the intersection

$\Delta \cap \Delta_i(\phi_i)$ $(i = 1, 2, 3)$. Hence the triplet $(\boldsymbol{\nu}, \boldsymbol{\eta}_i, x_i - z)$ is never coplanar, implying that $\boldsymbol{\nu} \cdot ((x_i - z) \times \boldsymbol{\eta}_i) \neq 0$ as long as $z(\phi_1, \phi_2, \phi_3) \neq x_i$ $(i = 1, 2, 3)$. It follows that p_1 and p_2 are the images under (5) of two types of contact forces. The first are forces $(f_1, f_2, f_3) \in S_1 \times S_2 \times S_3$ for which $z(\phi_1, \phi_2, \phi_3) = x_i$. These forces are mapped by (5) to endpoints of three-contact SSI segments. The second are forces on the boundary of $S_1 \times S_2 \times S_3$, given by $0 \times S_2 \times S_3 \cup S_1 \times 0 \times S_3 \cup S_1 \times S_2 \times 0$. These forces are mapped by (5) to endpoints of two-contact segments. Hence each SSS curve on the boundary of $\widetilde{\mathcal{R}}$ is bounded on both sides by two-contact and three-contact linear segments. □

References

[1] J. E. Bares and D. S. Wettergreen. DANTE II: technical description, results, and lessons learned. *Int. J. of Robotics Research*, 18(7):621–649, 1999.

[2] A. Bicchi. Hands for dexterous manipulation and robust grasping: A difficult road toward simplicity. *IEEE Trans. on Robotics and Automation*, 16(6):652–662, 2000.

[3] J.-D. Boissonnat, O. Devillers, and S. Lazard. Motion planning of legged robots. *SIAM J. of Computing*, 30(1):218–246, 2000.

[4] T. Bretl. Motion planning of multi-limbed robots subject to equilibrium constraints: The free-climbing robot problem. *Int. J. of Robotics Research*, 25(4):317–342, Apr 2006.

[5] T. Bretl and S. Lall. A fast and adaptive test of static equilibrium for legged robots. In *IEEE Int. Conf. on Robotics and Automation*, pages 1109 – 1116, 2006.

[6] T. Bretl and S. Lall. Testing static equilibrium for legged robots. *IEEE Trans. on Robotics*, 24(4):794–807, 2008.

[7] T. Bretl, S. Rock, and J.C. Latombe. Motion planning for a three-limbed climbing robot in vertical natural terrain. In *IEEE Int. Conf. on Robotics and Automation*, pages 2946–2953, 2003.

[8] J.-S. Cheong, K. Goldberg, M. H. Overmars, E. Rimon, and A. F. van der Stappen. Immobilizing hinged polygons. *Int. J. of Computational Geometry and Applications*, 17(1), 2007.

[9] H. Choset, K. Lynch, S. Hutchinson, G. Kanto, W. Burgard, L. Kavraki, and S. Thrun. *Principles of Robot Motion: Theory, Algorithms, and Implementations*. MIT Press, Cambridge, MA, 2005.

[10] A. Dandurand. The rigidity of compound spatial grid. *Structural Topology*, 10:41–56, 1984.

[11] P. G. de Santos, J. Estremera, E. Garcia, and M. Armada. Including joint torques and power consumption in the stability margin of walking robots. *Autonomous Robots*, 18(1):43–57, 2005.

[12] M. A. Erdmann. An exploration of nonprehensile two-palm manipulation. *Int. J. of Robotics Research*, 17(5), 1998.

[13] F. Fen, M. Shoham, and R. Longman. Lyapunov stability of force-controlled grasps with a multifingered hand. *Int. J. of Robotics Research*, 15(2):137–154, 1996.

[14] A. Ghasempoor and N. Sepehri. A measure of machine stability for moving base manipulators. In *IEEE Int. Conf. on Robotics and Automation*, pages 2249–2254, 1995.

[15] B. Goodwine and J. Burdick. Motion planning for kinematic stratified systems with application to quasi-static legged locomotion and finger gaiting. *IEEE Trans.on Automatic Control*, 18(2):209–222, 2002.

[16] V. Guillemin and A. Pollack. *Differential Topology*. Prentice-Hall, Inc., New Jersey, 1974.

[17] Li Han, J. C. Trinkle, and Z. X. Li. Grasp analysis as linear matrix inequality problems. *IEEE Trans. on Robotics and Automation*, 16(6):663–674, 2000.

[18] K. Harada, S. Kajita, K K. Kaneko, and H. Hirukawa. ZMP analysis for arm/leg coordination. In *IEEE/RSJ Conf. on Intelligent Robots and Systems (IROS)*, pages 75–81, 2003.

[19] K. Hauser, T. Bretl, J.-C Latombe, K. Harada, and B. Wilcox. Motion planning for legged robots on varied terrain. *Int. Journal of Robotics Research*, 27(11-12):1325–1349, 2008.

[20] K. Hirai, M. Hirose, Y. Haikawa, and T. Takenaka. The development of Honda humanoid robot. In *IEEE Int. Conf. on Robotics and Automation*, pages 1321–1326, 1998.

[21] D. W. Hong and R. J. Cipra. Optimal contact force distribution for multi-limbed robots. *J. of Mechanical Design*, 128(3):566–573, 2006.

[22] E. Krotkov and R. Simmons. Perception, planning, and control for autonomous walking with the Ambler planetary rover. *Int. Journal of Robotics Research*, 16:155–180, 1996.

[23] J. Kuffner, K. Nishiwaki, S. Kagami, M. Inaba, and H. Inoue. Motion planning for humanoid robots under obstacle and dynamic balance constraints. In *IEEE Int. Conf. on Robotics and Automation*, pages 692–698, 2001.

[24] J.-C. Latombe. *Robot Motion Planning*. Kluwer Academic Publishers, Boston, 1990.

[25] G. F. Liu, J. Li, and Z. X. Li. Coordinated manipulation of objects by multifingered robotic hand in contact space and active joint space. In *IEEE Int. Conf. on Robotics and Automation*, pages 3743–3748, 2002.

[26] P. Lötstedt. Coulomb friction in two-dimensional rigid body systems. *Zeitschrift fur Angewandte Mathematik und Mechanik*, 61:605–615, 1981.

[27] K. M. Lynch and M. T. Mason. Stable pushing: Mechanics, controllability, and planning. *Int. J. of Robotics Research*, 15(6):533–556, 1996.

[28] A. Madhani and S. Dubowsky. Motion planning of mobile multi-limb robotic systems subject to force and friction constraints. In *IEEE Int. Conf. on Robotics and Automation*, pages 233–239, 1992.

[29] D. W. Marhefka and D. E. Orin. Gait planning for energy efficiency in walking machines. In *IEEE Int. Conf. on Robotics and Automation*, pages 474–480, 1997.

[30] M. T. Mason and J. K. Salisbury Jr. *Robots Hands and the Mechanics of Manipulation*. MIT Press, Cambridge, MA, 1985.

[31] M. T. Mason and Y. Wang. On the inconsistency of rigid-body frictional planar mechanics. In *IEEE Int. Conf. on Robotics and Automation*, pages 524–528, 1988.

[32] R. Mason, J. W. Burdick, and E. Rimon. Stable poses of 3-dimensional objects. In *IEEE Int. Conf. on Robotics and Automation*, pages 391–398, 1997.

[33] J. M. McCarthy. *An Introduction to Theoretical Kinematics*. MIT Press, Cambridge, MA, 1990.

[34] R. B. McGhee and A. A. Frank. On the stability properties of quadruped creeping gaits. *Mathematical Biosciences*, 3, 1968.

[35] R. B. McGhee and G. I. Iswandhi. Adaptive locomotion of a multilegged robot over rough terrain. *IEEE Trans. Syst., Man, Cybern.*, SMC-9(4):176–182, 1979.

[36] K. Mirza and D. E. Orin. General formulation for force distribution in power grasps. In *IEEE Int. Conf. on Robotics and Automation*, pages 880–887, 1994.

[37] H. Montes, S. Nabulsi, and M. A. Armada. Reliable, built-in, high-accuracy force sensing for legged robots. *Int. J. of Robotics Research*, 235(9):931–950, 2006.

[38] W. Neubauer. Locomotion with articulated legs in pipes or ducts. In *Int. Conf. on Intelligent Autonomous Systems*, pages 64–71, 1993.

[39] V.-D. Nguyen. Constructing force-closure grasps. *Int. J. of Robotics Research*, 7(3):3–16, 1988.

[40] T. Omata and K. Nagata. Rigid body analysis of the indeterminate grasp force in power grasps. *IEEE Trans. on Robotics and Automation*, 16(1):46–54, 2000.

[41] Y. Or. *Frictional Equilibrium Postures for Robotic Locomotion: Computation, Geometric Characterization, and Stability Analaysis*. PhD thesis, Dept. of ME, Technion, Haifa, Israel, August 2007.

[42] Y. Or and E. Rimon. Computation and graphical characterization of robust multiple-contact postures in two-dimensional gravitational environments. *Int. Journal of Robotics Research*, 25(11):1071–1086, 2006.

[43] Y. Or and E. Rimon. On the hybrid dynamics of planar mechanisms supported by frictional contacts. I: Necessary conditions for stability. In *IEEE Int. Conf. on Robotics and Automation*, pages 1213 – 1218, 2008.

[44] J. S. Pang and J. C. Trinkle. Stability characterizations of fixtured rigid bodies with coulomb friction. In *IEEE Int. Conf. on Robotics and Automation*, pages 361–368, 2000.

[45] E. Papadopoulos and D. Rey. A new measure of tipover stability margin for mobile manipulators. In *IEEE Int. Conf. on Robotics and Automation*, pages 3111–3116, 1996.

[46] J. Park, K. Harada, and M. Kaneko. Enveloping grasp feasibility inequality. In *IEEE Int. Conf. on Robotics and Automation*, pages 2210–2216, 2001.

[47] J. Park and Y. Youm. General ZMP preview control for bipedal walking. In *IEEE Int. Conf. on Robotics and Automation*, pages 2682–2687, 2007.

[48] J. Ponce, S. Sullivan, A. Sudsang, J.-D. Boissonnat, and J.-P. Merlet. On computing four-finger equilibrium and force-closure grasps of polyhedral objects. *Int. J. of Robotics Research*, 16(1):11–35, February 1997.

[49] V. T. Rajan, R. Burridge, and J. T. Schwartz. Dynamics of rigid body in frictional contact with rigid walls. In *IEEE Int. Conf. on Robotics and Automation*, pages 671–677, 1987.

[50] J. R. Rebula, P. D. Neuhaus, B. V. Bonnlander, M. J. Johnson, and J. E. Pratt. A controller for the LittleDog quadruped walking on rough terrain. In *IEEE Int. Conf. on Robotics and Automation*, pages 1467–1473, 2007.

[51] T. Schlegl, M. Buss, T. Omata, and G. Schmidt. Fast dextrous regrasping with optimal contact forces and contact sensor-based impedance control. In *IEEE Int. Conf. on Robotics and Automation*, pages 103–108, 2001.

[52] N. Simaan and M. Shoham. Singularity analysis of a class of composite serial in-parallel robots. *IEEE Trans. on Robotics and Automation*, 7(3):301–311, 2001.

[53] T. Sugihara and Y. Nakamura. Contact phase invariant control for humanoid robot based on variable impedant inverted pendulum model. In *IEEE Int. Conf. on Robotics and Automation*, pages 51–56, 2003.

[54] M. Vukobratovic and B. Borovac. Zero moment point — thirty five years of its life. *Int. J. of Humanoid Robotics*, 1(1):157–173, 2004.

[55] M. Y. Wang. A full-kinematics model of fixtures for precision locating applications. In *IEEE/RSJ Int. Conference on Intelligent Robots and Systems (IROS)*, pages 1135–1140, 2001.

[56] Y. Wang and M. T. Mason. Two-dimensional rigid body collisions with friction. *J. of Applied Mechanics*, 10:292–352, 1993.

[57] B. H. Wilcox, T. Litwin, J. Biesiadecki, J. Matthews, M. Heverly, J. Morrison, J. Townsend, N. Ahmed, A. Sirota, and B. Cooper. ATHLETE: A cargo handling and manipulation robot for the moon. *J. of Field Robotics*, 24(5):421–434, 2007.

[58] J. J. Xu, G. F. Liu, and Z. X. Li. On quality functions for grasp synthesis and fixture planning. In *IEEE Int. Conf. on Robotics and Automation*, pages 333–338, 2004.

[59] K. Yokoi, F. Kanehiro, K. Kaneko, S. Kajita, K. Fujiwara, and H. Hirukawa. Experimental study of humanoid robot HRP-1S. *Int. J. of Robotics Research*, 23(4-5):351–362, 2004.

[60] Y. Yokokohji, S. Nomoto, and T. Yoshikawa. Static evaluation of humanoid robot postures constrained to the surrounding environment through their limbs. In *IEEE Int. Conf. on Robotics and Automation*, pages 1856–1863, 2002.

[61] T. Yoshikawa. Passive and active closure by constraining mechanisms. *J. of Dynamic Systems, Measurement, and Control*, 121 (3-4):418–424, 1999.